(2)

主論文

Differential Cross Sections for the np → dX Reaction at 1.0 and 2.0 GeV

Shin'ya Sawada

A dissertation submitted in partial fulfillment of

the requirements for the degree of

Doctor of Science

Department of Physics

Kyoto University

1997

Abstract

Inclusive deuteron spectra ($d^2\sigma/d\Omega dp$) have been measured for the reaction, np $\rightarrow$ dX, at neutron energies of 1.0 and 2.0 GeV. The present data provide the inclusive deuteron formation cross section at the highest energy so far measured. A quasi-monochromatic neutron beam was used along with a liquid hydrogen target. Recoil deuterons at laboratory angles from 3° to 15° were tracked in wire chambers surrounding a 1.5 T·m dipole magnetic field. Particle identification was achieved using time-of-flight and momentum measurements. The momentum spectra of deuterons are compared with the prediction of a one-nucleon-exchange model with σ meson production. At 2 GeV, the missing mass spectra suggest the large role played by both the η and ρ mesons in deuteron production.

Contents

List of Tables

List of Figures

Chapter 1

Introduction

The np $\rightarrow$ dX reaction is the simplest nuclear reaction and a knowledge of the details of the reaction mechanism over a wide range of energies is indispensable. This reaction is also suited to study nuclear-meson picture of the strong interaction. Especially in the few GeV region, the np $\rightarrow$ dX reaction has been rarely studied previously.

The missing particles in the np $\rightarrow$ dX reaction are able to have I (isospin) = 0 and 1, while only I=1 is allowed in the pp $\rightarrow$ dX reaction. Therefore, I=0 particles, or the I=0 multi-particle final state can uniquely contribute to the np $\rightarrow$ dX reaction. Below the threshold of two-pion production, the np $\rightarrow$ dX reaction is dominated by the np $\rightarrow$ dπ^0 process. When the energy extends above the threshold of two-pion production ($T_n \simeq 0.6$ GeV), the phase space is rapidly enlarged and the np $\rightarrow$ d$\pi\pi$ process plays a large role. Moreover, in the energy region above the η (I=0) and ρ (I=1) thresholds ($T_n = 1.25$ and 1.85 GeV, respectively), the np $\rightarrow$ dη and dρ processes could make important contributions to inclusive deuteron production. Thus the reaction mechanism including η and ρ meson production can be investigated at 2 GeV for the first time.

1.1 Previous Data on the np $\rightarrow$ dX Reaction

Many experiments on the nucleon-nucleon interaction in the few GeV region have been carried out, but most of them used a proton beam because a neutron beam with narrow energy spread was not easy to obtain. Data on the neutron-proton interaction with deuteron formation are especially scarce.

Experiments on the neutron-proton interactions with deuteron formation at energies of a few GeV were first studied with bubble chambers. Bar-Nir *et al.* [1] studied the $np \rightarrow d\pi^+\pi^-$ reaction below 2.7 GeV. They used a neutron beam with a continuous energy distribution produced by 4.5 GeV electrons hitting a Be target. Their data were divided into three incident energy regions with roughly 570 events in each region ($T_n < 1.12$ GeV; 1.12 GeV $\leq T_n < 1.32$ GeV; and $T_n \geq 1.32$ GeV). An analysis was made of the data from each of these regions. They measured the angular distribution of deuterons and pions, the invariant mass spectra of the two-pion system, the opening angle distribution of a deuteron and a pion, and the opening angle distribution of two-pions. They reported some excess around 0.3 GeV in the invariant mass spectra and labeled this the ABC peak. The ρ^0 was apparently absent in the invariant mass ($M_{\pi^+\pi^-}$) spectra. The one-pion-exchange model was applied with two different diagrams. Although the model had been successful in explaining the $pp \rightarrow d\pi^+$ reaction, it could not reproduce all of the spectra mentioned above simultaneously. Since the statistical accuracy was poor, and the incident neutron momentum was not definite, these data could not establish the existence of the ABC peak. Likewise the absence of the ρ^0 peak and the poor agreement with the one-nucleon-exchange model were only suggested by the data.

Abdivaliev *et al.* [2] carried out an experiment with fixed-energy neutron beams of 1.03 GeV and 1.48 GeV and a hydrogen bubble chamber. They provided the invariant mass plots ($M_{\pi^+\pi^-}$ and $M_{d\pi^\pm}$), the momentum distributions in the center-of-mass system ($P_{\pi^\pm}$ and P_d), the scattering angle distributions of the $\pi^\pm$ and the deuterons, and the opening angle of the two- pions. Since the absolute cross section was not provided, comparison of the data with theoretical calculations was not quantitative.

The first high quality experimental data on neutron-proton interactions with deuteron formation using a magnetic spectrometer were taken at Saclay. By the end of 1970, a neutron beam up to about 1.2 GeV was developed at Saclay by stripping deuterons extracted from the synchrotron Saturne. This neutron beam line had been the highest energy narrow band beam before the new neutron beam line at the KEK-PS was constructed for the present experiment. Plouin *et al.* [3] measured deuteron momentum spectra with the neutron beam of 1.2 GeV. They provided the momentum spectra at $\theta_d^{lab} = 0°$, 4.5°, 7.5° and 10.5°. Especially at forward angles, they observed

remarkable bumps near the two-pion threshold (so-called "ABC peaks"), and a bump in the region of the largest kinematically allowed missing mass. In a subsequent paper [4], they showed the bump in the largest missing mass region was due to the np $\rightarrow$ dη reaction.

ABC effect The so-called ABC peak was first observed by Abashian *et al.* [5] in the momentum spectra of ^{3}He produced in p-d collisions with $T_p \sim 0.745$ GeV. They argued that the bump in the observed ^{3}He momentum spectrum was due to the I=0 $\pi\pi$ interaction in the isoscaler channel.

Many efforts followed to investigate this ABC effect. These investigations, especially those on the dp $\rightarrow$ ^{3}HeX reaction [6], strongly suggested that the ABC anomaly was not a resonance, but linked strongly with the reaction mechanism. This followed because the mass position of the ABC effect changed significantly with kinematical conditions and the production cross section was strongly dependent on the emission angle of the ^{3}He and on the total energy of the reaction. Since the ABC effect is related with I=0 $\pi\pi$ interaction, the simplest reaction is np $\rightarrow$ d$\pi\pi$ and a few measurements have been carried out for the np $\rightarrow$ dX reaction. Hollas *et al.* [7] measured the deuteron spectra from the initial state of n + p at $T_n = 0.8$ GeV. They did not observe any peaks near the $\pi\pi$ threshold, while Plouin *et al.* [3] working at 1.2 GeV reported the existence of the ABC peaks in their inclusive deuteron spectra. These results also confirmed that the ABC effect was not a resonance. The investigation on the reaction mechanisms at this energy region is indispensable to understand the mechanism the ABC effect quantitatively.

1.2 Theoretical Models

Several theoretical models of the np $\rightarrow$ dX reaction have been presented. Yoshino *et al.* [8] calculated the double-differential cross sections ($d^2\sigma/d\Omega dp$) for the np $\rightarrow$ dX reaction with the diagram shown in Fig. 1.1(a). In this one-nucleon-exchange model, one of the nucleons in the initial state emits a σ meson which decays into two pions. The nucleons then form a deuteron. In this model, the I=0 s-wave $\pi\pi$ phase shift was used instead of the mass and the width of the σ meson. They adjusted the s-wave $\pi\pi$

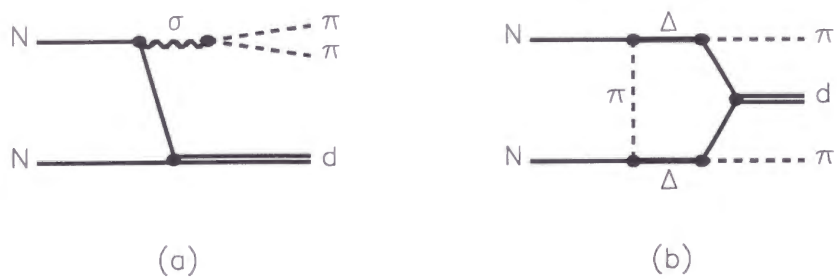

Figure 1.1: Diagrams included in the theoretical calculations: (a) One-nucleon-exchange model of Yoshino *et al.*; (b) $\Delta\Delta$ model of Bar-Nir *et al.*

phase shift and the coupling constant at the NNσ vertex (g_σ) in order to simultaneously reproduce the measured momentum spectra at T_n = 0.8 GeV [7] and 1.2 GeV [3]. As a result of the adjustment, they could reproduce the momentum spectra at T_n = 0.8 GeV well, while the calculated spectra underestimated the experimental data at T_n = 1.2 GeV. It should be noted that only the I=0 state of two π's in the final state is taken into account because only the σ production is considered. According to the $\pi\pi$ phase shift analysis [9, 10, 11, 12], the I=1 phase shift in this energy region is much smaller than the I=0 phase shift.

One of the other models is the $\Delta\Delta$ model by Bar-Nir *et al.* [13, 14] as shown schematically in Fig. 1.1(b). In this model, two Δ resonances are considered as an intermediate state and a deuteron is formed after they each decay into N + π. They argued that the ABC peak in the NN $\rightarrow$ d$\pi\pi$ reaction (the peak near the two-pion threshold) corresponded to parallel decay of the two Δ excitations and that the bump in the largest missing mass region was due to anti-parallel decay of the two Δ's. Their results show striking ABC peaks in the calculated momentum spectra, but they failed to reproduce the experimental results at T_n = 1.2 GeV. The $\Delta\Delta$ model includes the I=1 state as well as the I=0 state, but these results showed that the contribution from the I=1 state is negligibly small.

Purpose of the present experiment The mechanism of the np $\rightarrow$ dX reaction is not fully understood in the energy region near and above 1 GeV. In the energy region around 1 GeV, the ABC effect should be investigated through the reaction mechanism of the two pion interaction. In this region, information on the energy dependence of the ABC effect can be used to improve the theoretical models. Above the η and ρ thresholds (1.25 and 1.85 GeV, respectively), these contributions should also be included. Plouin *et al.* [4] suggested that the np $\rightarrow$ dη reaction contributed to the np $\rightarrow$ dX reaction, but because only a part of the neutron beam was above the threshold of η production, a quantitative treatment of their data seems to be difficult. The bubble chamber data of the np $\rightarrow$ d$\pi^+\pi^-$ reaction by Bar-Nir *et al.* [1] did not see ρ^0's.

After the success of the deuteron acceleration at KEK-PS, an experiment with a neutron beam line of the highest energy was made possible. The present investigation intends to shed light on the mechanism of the np $\rightarrow$ dX reaction at 1.0 and 2.0 GeV, using this new neutron beam. Proton and deuteron spectra in neutron-proton interactions were measured with the highest energy neutron beam and a large acceptance spectrometer. The experimental results will be compared with the calculations based on the one-nucleon-exchange model.

Contents of this paper In Chapter 2 of this paper the experimental apparatus used for these measurements is described. Chapter 3 describes the methods of data analysis, and the results and interpretation of these data are presented in Chapter 4. Our conclusions are presented in Chapter 5.

Chapter 2

Experimental Apparatus

2.1 Overview

This experiment was carried out using the P1 beam line at the proton synchrotron of the National Laboratory for High Energy Physics (KEK-PS). At the end of 1992, the deuteron beam was successfully accelerated and used in an experiment (APEX, KEK-PS E257) for the first time at the KEK-PS. After this success, the quasi-monoenergetic neutron beam from deuteron breakup was made available. The neutron beam line was designed and constructed specifically for this experiment [15]. Neutron beams with centroid energies of 1.0 and 2.0 GeV were incident on a liquid hydrogen target. Protons and deuterons produced by the reaction were analyzed by a magnetic spectrometer and time-of-flight scintillator arrays. The spectrometer accepted particles in a wide range of scattering angles. For example, deuterons were observed up to 90° in the n-p center-of-mass system. A neutron beam monitor (NBM) was developed to monitor the neutron beam profile and intensity [16].

In the subsequent sections, details of the experimental setup are presented.

2.2 Neutron Beam

Deuterons accelerated by the KEK-PS were slow-extracted over about 1.5 sec., during 4 sec. spill time, to the P1 line at the east counter hall (Fig. 2.1). The deuteron beam was incident on a 6 cm long Be target, where the neutrons were produced by the deuteron breakup reaction. The neutrons produced at around 0° were used for the

neutron beam. The non-interacting deuterons and other charged particles produced at forward angles were swept away with a dipole magnet (D2). Following the sweeping magnet, the neutron beam was defined with a 5 m long lead collimator of square cross section surrounded by an iron absorber. The width of the collimator was 34 mm at the entrance and gradually widened to 52 mm at the exit in order to reduce the secondary particle production. The solid angle of the collimator was 50 μsr. The beam divergence determined by the collimator was $\pm 0.2°$. Since the energy range of the available deuteron beam at the KEK-PS is from 2 to 11.2 GeV, the neutron beam line was designed to provide the neutron beams from 1 to 5.6 GeV.

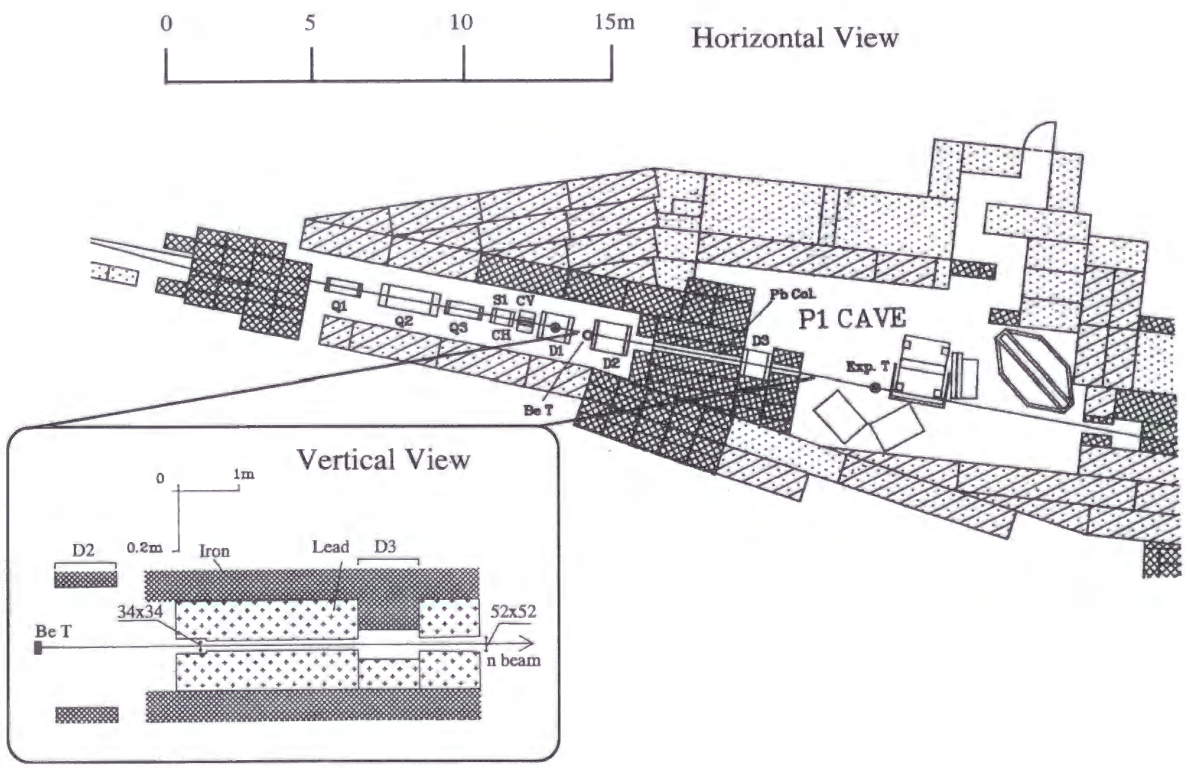

Figure 2.1: The P1 beam line at the KEK-PS showing the Be production target (Be T), charged particle sweeping magnet (D2), neutron collimator (Pb Col.), and the P1 experimental cave.

A similar neutron beam line has been constructed at Saclay [17] with the maximum neutron energy of 1.2 GeV. At this energy they measured the forward-angle neutron production cross sections for various kinds of target materials (Be, C, Al, Cu, and

Pb). Be was found to be the highest yield neutron production target. We prepared three samples of production targets of Be of 3 cm, 6 cm, and 10 cm length. The neutron production rates of the three targets were measured. The 6 cm and 10 cm targets had the same neutron yield. Because the energy lost by a deuteron in the production target should be small in order to get the neutron beam of good energy resolution, and interactions of neutrons with target material should be suppressed, a shorter target is preferred. Therefore a 6 cm long Be target was used.

The collimator defined the neutron beam profile at the liquid hydrogen target located 9.85 m downstream from the Be target. The size of the collimator was determined to obtain a tolerable beam size at the hydrogen target and optimal beam intensity. The liquid hydrogen was contained in a vertical cylinder of 120 mm diameter and the projected beam size at the target was designed to be 70 mm square.

The spatial distribution of the neutron beam at the hydrogen target was measured by the neutron beam monitor at an early stage of the construction of the experimental apparatus when the spectrometer was not yet fully instrumented. Figure 2.2 shows x- and y-projections of the charged particle tracks at the hydrogen target. The x-projection is not square because the hydrogen target was a vertical cylinder. The neutron beam was 70 mm $\times$ 70 mm, which was well within the hydrogen target because the hydrogen target was 12 cm in diameter. This neutron distribution corresponded to the solid angle of 50.5 μsr as designed.

The performance of the neutron beam line was simulated with a Monte Carlo code GEANT [18]. In order to obtain the neutron momentum distribution in a deuteron, Hulthén's wave function was used,

$$\psi(r) = \sqrt{\frac{\alpha}{\pi}} \frac{e^{-\alpha r}}{r}, \tag{2.1}$$

where r represents the relative distance between the two nucleons and $\alpha^{-1} = 4.3$ fm ($\alpha\hbar = 46$ MeV/c) was used. From the Fourier transformation of ψ, the neutron momentum distribution in the deuteron rest frame is written as,

$$f(p^*)dp^* = C\frac{p^{*^2}}{[p^{*^2} + (\alpha\hbar)^2]^2}dp^*, \tag{2.2}$$

where C represents a normalization factor and p^* is the momentum in the deuteron rest frame. In the Monte Carlo code, neutrons were assumed to have the momentum

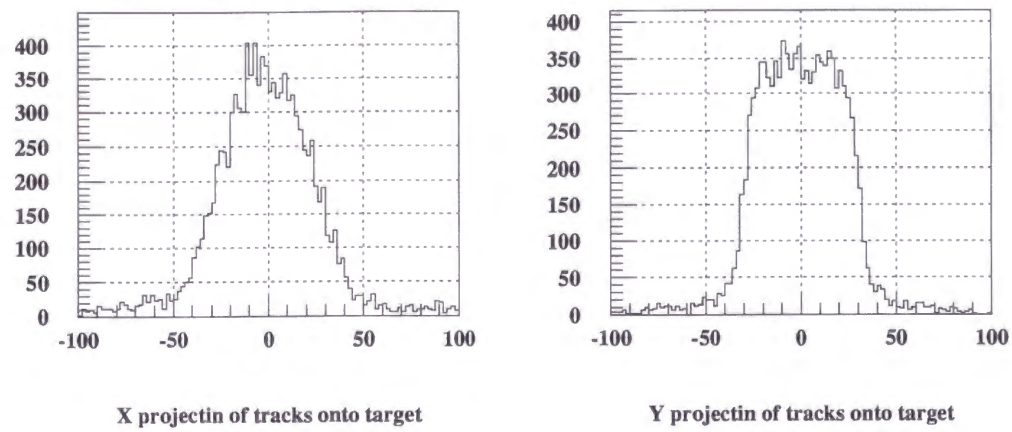

Figure 2.2: x- and y-projection of charged particle tracks at the median plane of the liquid hydrogen target, showing the neutron beam profile. Units are mm. The horizontal distribution is more rounded than the vertical distribution due to the cylindrical shape of the hydrogen target. It should also be noted that the errors of the x-projection are larger than those of the y-projection.

distribution expressed by Eq. 2.2. The simulation also took into account the effects of: (i) the straggling of the deuteron energy loss and multiple scattering in the Be target (6 cm), and (ii) the energy spread of the deuteron beam ($\sigma \sim 3\%$). Materials along the neutron path (collimator and air) were also included in the code, in order to simulate the effects of the materials such as the scattering and particle production on the surface of the collimator and in the air, etc. The calculated momentum distribution of the neutron beam at the hydrogen target is shown in Fig. 2.3. The solid lines in the figure are results of a fit to the simulated spectra with a function,

$$F(p)dp = C\frac{\gamma_d^3 p^2}{[(p-p_c)^2 + (\gamma_d \alpha\hbar)^2]^2}dp, \tag{2.3}$$

where $\gamma_d = (1-\beta_d^2)^{-1/2}$, where β_d is the deuteron velocity and p_c is the central value of the neutron beam momentum distribution. The function $F(p)$ corresponds to the Lorentz transformation of the longitudinal component of $f(p^*)$, in which $p^* = (p-p_c)/\gamma_d$. The fact that the simulated spectra are well fitted by $F(p)$ which includes only the Fermi motion implies that the effects other than the Fermi motion of a neutron in a deuteron can be neglected. Thus the momentum distribution function

$F(p)$ can be used as the function which represents the momentum distribution of the neutron beam produced at 0°. The momentum spread of the simulated neutron beam was 7.2% in FWHM at $T_n = 1$ GeV, which was consistent with that obtained by the measurement of the charge exchange process (np $\rightarrow$ pn) with the spectrometer as discussed in Chapter 3.

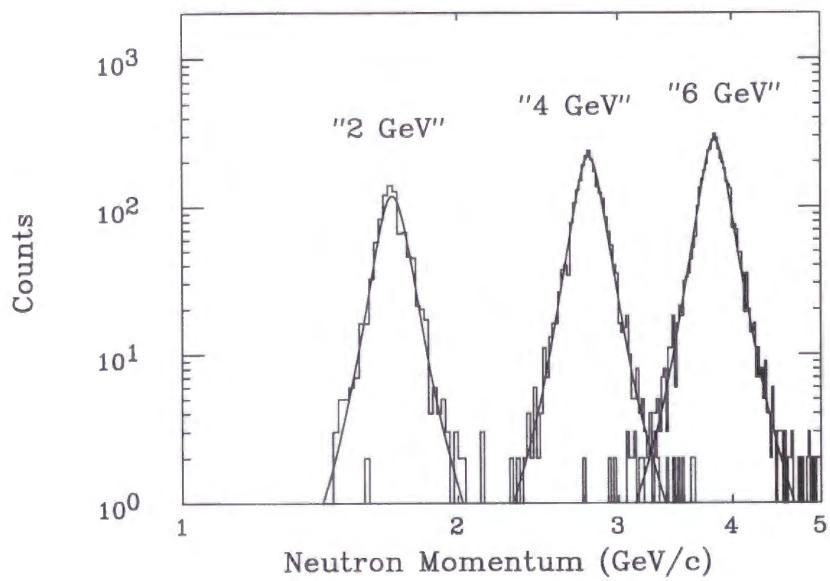

Figure 2.3: The neutron momentum spectra obtained by Monte-Carlo simulations of proton stripping reactions for deuterons in the beryllium target. The quoted energies (2, 4, and 6 GeV) indicate the deuteron beam energy used in the simulation. The solid lines show fits to the spectra with a function of the form of eq. (2.3).

The deuteron beam intensity was measured with the secondary emission chamber (SEC) [19] located upstream of the Be target. The SEC is an ionization chamber using an aluminum foil as a radiator, which emits secondary electrons. The SEC was calibrated using the foil activation method [19, 20]. The number of ^{24}Na nuclei produced by the ^{27}Al(d,3p2n)^{24}Na reaction was determined from the measured yield of 1368.5 keV gamma rays measured from ^{24}Na after irradiated with deuterons. There are two values of the measured cross section for the ^{27}Al(d,3p2n)^{24}Na reaction: 15.25 $\pm$ 1.5 mb at $T_d = 2.33$ GeV [21], and 14.7 $\pm$ 1.2 mb at $T_d = 7.3$ GeV [22]. From these data, the cross section of the Al(d,3p2n)^{24}Na reaction was assumed to be 15.0 $\pm$ 1.5 mb and constant within our beam energies for the evolution of the number of incident

deuterons. Errors which should be considered were 5% on the detection efficiency of gamma rays, 1% on the statistical uncertainty of the gamma-ray measurement, < 1% on the thickness of the aluminum foil and 10% on the cross section. Thus the overall uncertainty for the number of the incident deuterons was about ±11%.

In order to estimate the neutron flux from the measured deuteron beam intensity, the production efficiency of neutrons from deuterons should be given. The differential cross sections for d + $^9Be \rightarrow$ n + X at 0° in the several GeV region have been reported at the neutron momenta of 1.35, 1.77, and 2.90 GeV/c [23]. Fitting the data with a linear function of the neutron momentum p_n (in GeV/c), the differential cross section (in barn/sr) is expressed as,

$$\frac{d\sigma}{d\Omega}(\theta = 0°) \simeq 24 \cdot p_n - 10. \tag{2.4}$$

The neutron production efficiency (η) is defined by the ratio of the number of neutrons (N_n) to the number of incident deuterons (N_d) as,

$$\eta = \frac{N_n}{N_d} = N_{Be}\frac{d\sigma}{d\Omega}(\theta = 0°)\Delta\Omega, \tag{2.5}$$

where N_{Be} is the areal number density of beryllium nuclei in the target and $\Delta\Omega$ is the solid angle of the neutron collimator (50 μsr). Because the neutron momentum distribution was well described at 0° by the distribution function F(p), cross sections only at 0 degrees were considered. The transformation efficiencies from deuterons to neutrons are shown in Table 2.1. The errors include uncertainties due to the deuteron beam intensity with the foil activation method and the statistical errors of the fit to the previous data of the neutron production cross sections on the Be target. Typically, 1×10^8 neutrons per sec. were delivered to the hydrogen target during the experiment.

Table 2.1: Neutron production efficiency (η).

T_d (GeV)	T_n (GeV)	η
2.0	1.0	$(1.16 \pm 0.31) \times 10^{-3}$
4.0	2.0	$(2.14 \pm 0.58) \times 10^{-3}$
4.7	2.35	$(2.46 \pm 0.67) \times 10^{-3}$
5.4	2.7	$(2.79 \pm 0.75) \times 10^{-3}$
6.0	3.0	$(3.07 \pm 0.84) \times 10^{-3}$

A thin plastic scintillator was located at the entrance of the experimental area

(P1 cave) as a veto counter for charged particles contaminating the neutron beam. The counter was 100 mm in both width and height, and of 2 mm thickness.

2.3 Neutron Beam Monitor

A neutron beam monitor (NBM) was constructed for this experiment. The NBM was used to measure the neutron beam profile at the hydrogen target at the beginning of the experiment, and to provide an alternative way to measure the neutron beam intensity in order to check the one calculated from the measured deuteron beam intensity.

The NBM consisted of three planes of plastic scintillation hodoscopes (Fig. 2.4). The first plane, of 2 mm thickness, was used as a veto for incident charged particles, while the 10 mm thick second plane sampled the incident neutron beam through neutron-proton and neutron-nucleus reactions inside the scintillators. The third plane was oriented at right angles to the scintillator strips of plane 2. Planes 2 and 3 then provided an x-y profile of the neutron beam with a bin size of 20 mm.

Two methods were applied to measure the neutron beam intensity: one from the measurement of the deuteron beam intensity using the SEC, and one using the NBM. In Fig. 2.5, the detection efficiency of neutrons of the NBM is plotted.

The procedure to evaluate the detection efficiency from the measurement of the deuteron beam intensity (open circles in the figure) was as follows:

1. the deuteron beam intensity was measured with the SEC,
2. the neutron beam intensity was evaluated from the deuteron beam intensity with the transformation efficiency described in Sec. 2.2 (Table 2.1),
3. the number of neutron counts was obtained with the NBM,
4. the ratio of the number of neutrons obtained in the step 3 to that obtained in the step 2 was defined as the detection efficiency.

The neutron detection efficiency of the NBM was modeled with the GEANT code using several hadronic interaction packages. In the simulation code, neutrons were

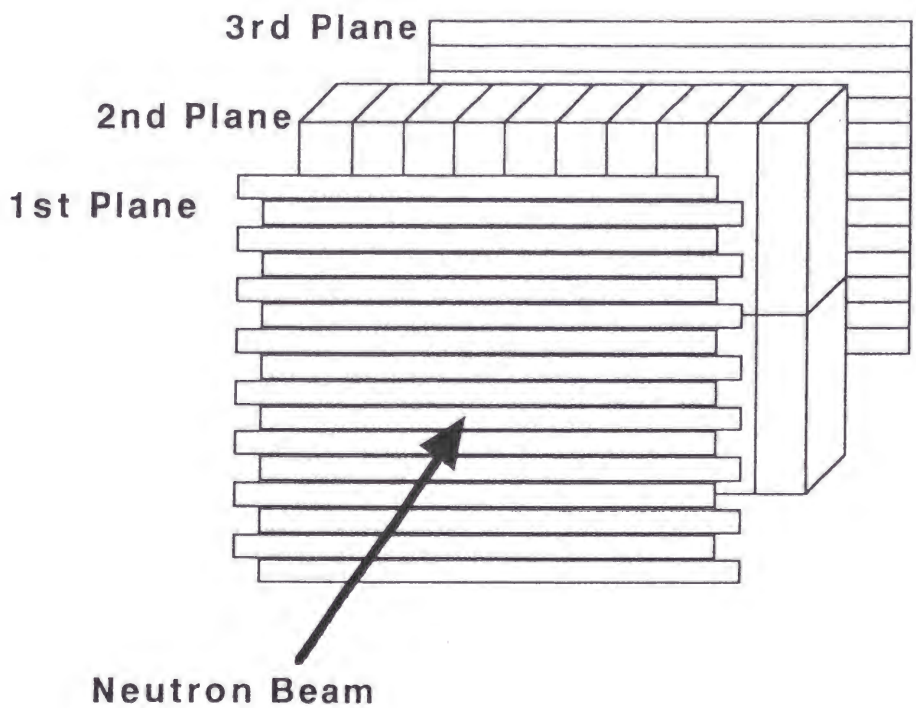

Figure 2.4: A schematic view of the neutron beam monitor.

incident on the NBM and the interaction of neutrons with the plastic scintillators was simulated. Charged particles produced by the interaction deposited energy in the NBM and the number of events with total ionization above the same threshold as the hardware condition were counted. The ratio of the number of detected counts to the number of incident neutrons was defined as the detection efficiency. In Fig. 2.5 the efficiency results using three hadronic interaction packages (GHEISHA, TATINA, and FLUKA) are plotted with solid markers.

At each of the beam energies except for $T_n = 1$ GeV, the results of two methods showed agreement at the level of about 20%. Even at the beam energy of $T_n = 1$ GeV, the results were within the uncertainties of the transformation efficiency.

Because results of these two methods showed agreement, the neutron beam flux derived from the measured deuteron beam intensity has been used to evaluated the cross sections, as discussed in Chapter 3. The neutron beam flux obtained in this way is confirmed by comparing our measured np $\rightarrow$ pn charge-exchange cross sections with previous results.

2.4 Hydrogen Target

A liquid hydrogen target system was constructed specifically for this experiment (Fig. 2.6). The hydrogen cell was a vertical cylinder with 120 mm diameter and 150 mm height. The wall of the cell was made of stainless steel with a thickness of 0.1 mm. The vacuum vessel consisted of a vertical stainless steel cylinder of 3 mm thickness. This was reduced to 0.15 mm in the direction of the charged particle spectrometer arm.

The hydrogen temperature and pressure were continuously monitored to maintain a constant target density. Averaged over the known neutron beam spot at the target location, the hydrogen thickness was 0.815 g/cm^2. Target-full and target-empty data were sequentially collected at each beam energy to subtract the backgrounds from materials other than hydrogen.

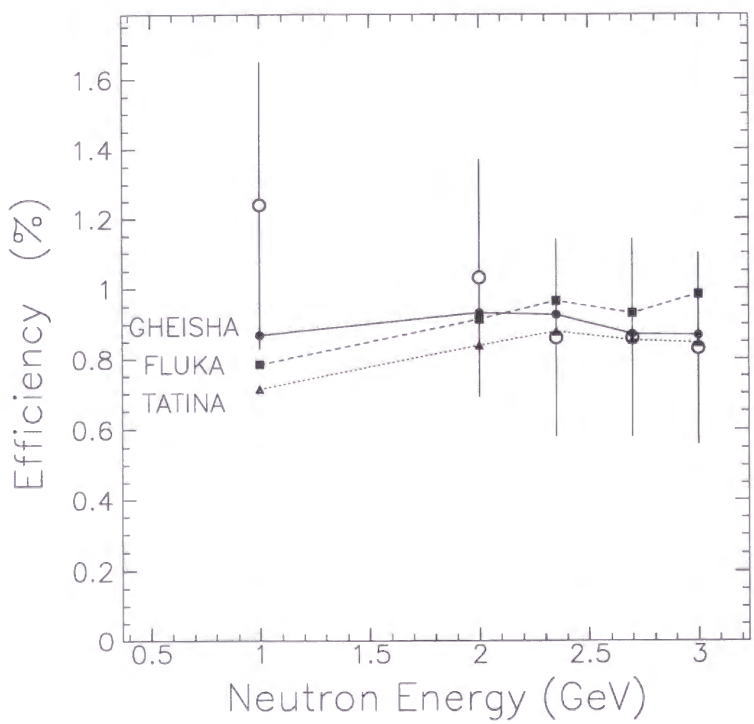

Figure 2.5: Detection efficiencies for the NBM as a function of the neutron momentum (solid markers) obtained with the GEANT simulations using three hadronic interaction codes. The open circles show the measured efficiencies from the known deuteron intensity.

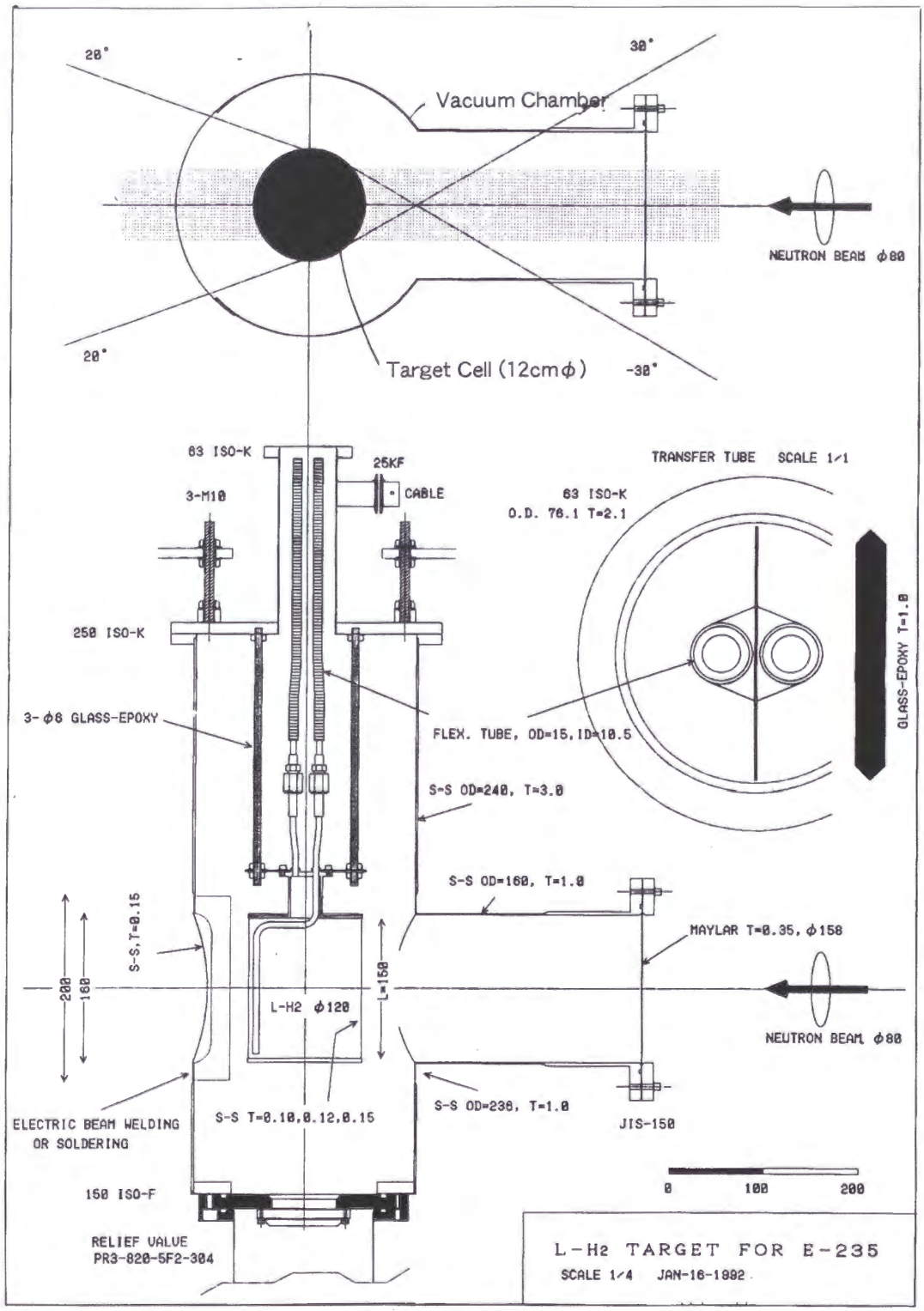

Figure 2.6: Layout of the liquid hydrogen target system. Units are mm.

2.5 Recoil Spectrometer

Charged particles from the target were detected with a magnetic spectrometer system. The spectrometer consisted of sets of segmented scintillators (RS1, 2, 3, and 4), multiwire proportional chambers (MWPC's, PC1 and 2), and drift chambers (DC1 and 2), configured around a 1.5 T·m large-gap dipole magnetic field, as shown in Fig. 2.7. The detector arms shown to the right of the beam line in Fig. 2.7 were used to detect high energy gamma rays in coincidence with charged particles. These detectors were used in another part of the experiment.

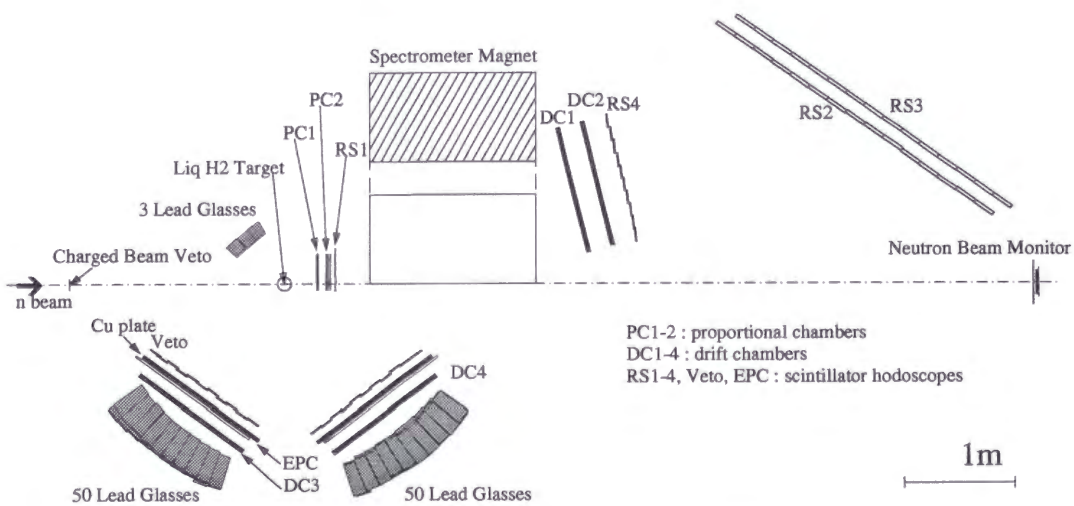

Figure 2.7: The detector layout used for experiment E235. The neutron beam is incident from the left, and passes through the hydrogen target as well as the wire chambers PC1, PC2 and the scintillator RS1. The lead glass detectors were used to detect gamma rays in coincidence with recoil particles and are not considered in the present analysis.

2.5.1 Spectrometer Magnet

The spectrometer magnet was modified from a C-type magnet called the K-μ magnet. The gap was enlarged to 40 cm and extra coils and return yokes were added. The pole was 80 cm in width and 150 cm in length. The magnetic field at the center of the pole was 10 kG. The magnetic field was measured by Hall probes with the grid size of 20 mm $\times$ 30 mm $\times$ 20 mm (Fig. 2.8). A stationary NMR probe was used

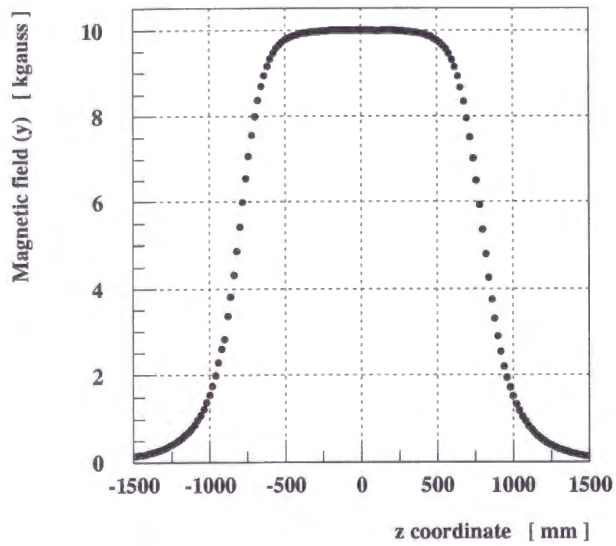

Figure 2.8: A field map in the scattering mid-plane. The y (vertical) component of the magnetic field along the beam axis along the center of the pole is plotted.

during the measurement and the production runs to insure field reproducibility and stability.

2.5.2 Drift Chambers

DC1 and DC2 were constructed and used by the K_L group for their experiment KEK-PS E137. DC1 and DC2 were identical with each other, each consisting of four 128-wire planes (x, x', y, and y') with 9 mm sense wire spacing. Alternate planes were laterally staggered by 4.5 mm, as shown in Fig. 2.9. Each drift cell had a honeycomb structure. The sense wires were made of gold-plated tungsten with a diameter of 20 μm and strung with a tension of 40 g. The field wires were made of gold-plated aluminum with a diameter of 100 μm and strung with a tension of 80 g. The high voltage supplied to the field wires was -2.0 kV, and the drift velocity was about 50 μm/nsec. The drift chambers were operated with the gas mixture of 50% argon and 50% ethane. There was a guard-wire plane at each of the outermost sides of the chamber, where the field wires were strung perpendicular to the sense wires and had

a potential of -1.85 kV. This was to make the electric field inside the cell symmetrical and to prevent electrons from entering from the outside.

The drift time for each wire was digitized with time-to-digital-converter (TDC) modules (TKO-Dr.T), with a resolution of 0.7 nsec per channel. The TDC's were operated with common stop mode, and t_0, the drift time offset (corresponding to tracks passing very close to the sense wire), was determined from the tdc spectra for each wire. Figure 2.10 shows an example of a spectrum. The edge of the distribution was fitted with a Gaussian plus constant, and the channel with a yield corresponding to 0.3 of the Gaussian peak amplitude was defined to be t_0.

Because the drift chambers were located at the region of nearly no magnetic field, the hits on the planes could be fitted with a straight line with the same way as for a magnet-off run. Four positions for each of x (horizontal) and y (vertical) coordinates were available for DC1 and DC2 and the dependence of the drift time on the position was determined with iterations of the procedure below: (i) a hit position on a plane was estimated with a straight-line fit of other three x (y) positions, (ii) the drift time which depended on the position was fitted with a third-order polynomial, (iii) steps (i) and (ii) were applied for all four x (y) planes and the process (i) was done again with a new function of the drift time on the position. The iterations were ended when the difference between the new reduced χ^2 and the previous one was apparently small ($= 0.0016$). A result of the iterations for the x plane of DC1 for a magnet-off run is shown in Fig. 2.11.

The position resolution of the drift chambers was estimated with a magnet-off run. Four positions for each of x (horizontal) and y (vertical) coordinates were available, three of which were fitted with a linear function and the residual was calculated for the forth plane in the same way as was applied to get the function of the drift time. Figure 2.12 shows a residual distribution; from these data, 320 μm was deduced as the RMS position resolution (σ).

The detection efficiency for each plane was evaluated in a similar way as the position resolution. Three x or y positions were fitted with a straight line and the hit position on the forth plane was estimated. The position-dependent detection efficiency was defined as the ratio of the number of actual hits around the expected

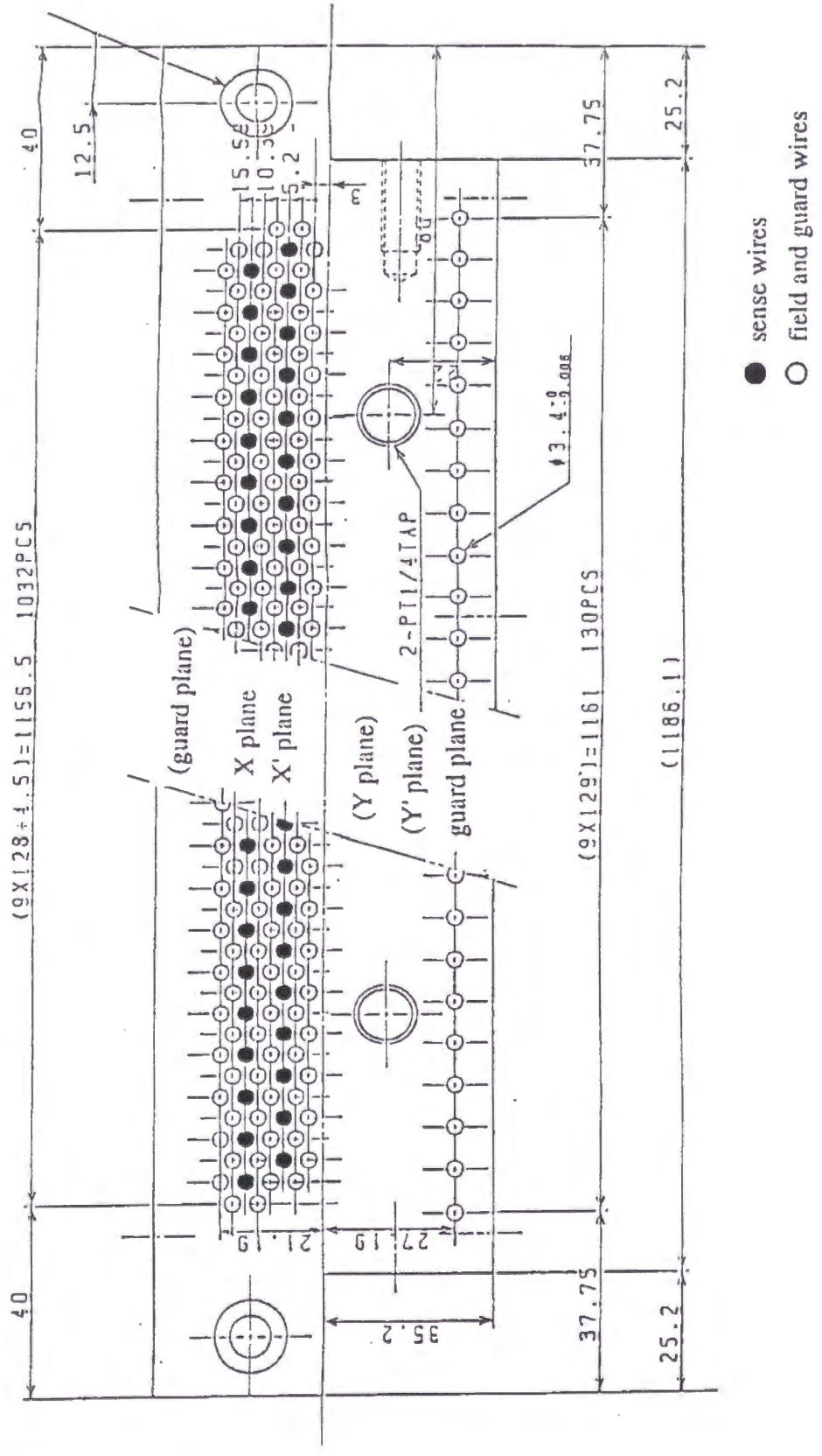

Figure 2.9: The layout of the drift chambers.

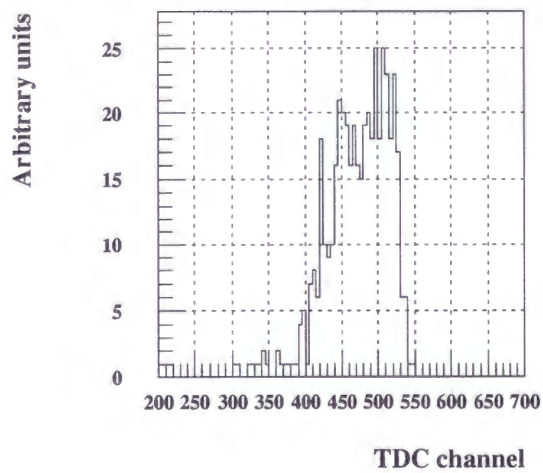

Figure 2.10: A typical TDC spectrum of the drift chamber.

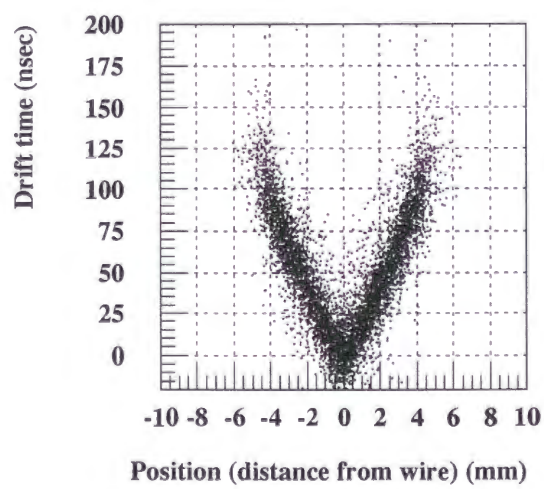

Figure 2.11: The drift time (vertical axis) versus the hit position (horizontal axis). Data were accumulated for all the wires of DC1, plane 1 (x).

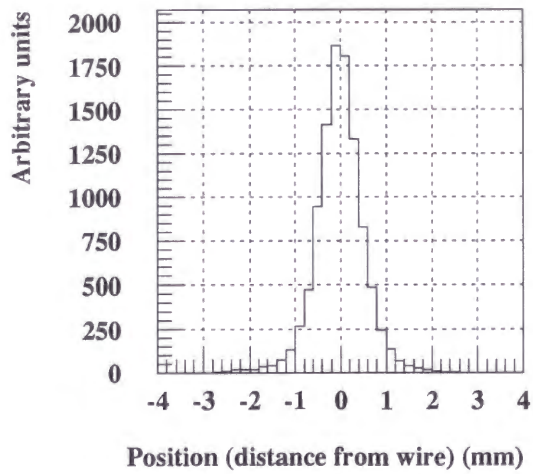

Figure 2.12: The distribution of x-residual in DC1.

position to the number of estimated hits. The typical detection efficiency averaged over each plane during the production runs was 95% for each of the DC1 planes, 73% for DC2-x planes, 92% for DC2-y plane and 90% for DC2-y' plane. These values were put into a Monte Carlo code to obtain the momentum-dependent efficiency function at each beam energy.

2.5.3 Multiwire Proportional Chambers

PC1 and PC2 were positioned between the liquid hydrogen target and the spectrometer magnet. A part of the effective area of these chambers was crossed by the neutron beam. PC2 was made by the E176 (KEK-PS) group, whereas PC1 was newly designed and constructed especially for use at high counting rate. Table 2.2 lists the geometry of these chambers and the wire spacings. The wire spacing of PC1 was 1 mm in order to compensate the space charge effect. The data from coupled pairs of adjacent wires were collected in order to reduce the required number of readout modules. The data readout was carried out with a SPIDER system, which was designed and constructed at KEK.

Table 2.2: Configuration of the chambers.

	planes	effective area	wire spacing	read-out
PC1	x,u,v	319 mm × 155 mm	1 mm	2 mm
PC2	x,y,u	320 mm × 192 mm	2 mm	2 mm
DC1,2	x,x',y,y'	115 cm × 115 cm	9 mm	

A so-called magic gas, which was a mixture of Ar, freon (CF_3Br), C_4H_{10} and methylal with the mixing ratio of 73:24:0.5:3, was used. The high voltage of -3.8 kV was supplied for the cathode planes.

The detection efficiency of each of the planes was typically 96%. Because the analysis program required hits in two planes out of three for each MWPC, the overall detection efficiency was more than 99%.

2.5.4 Time-of-flight Counters

RS1, RS2 and RS3 were used for the time-of-flight (TOF) measurements, whereas the RS4 scintillator array was used in order to reduce the accidental backgrounds especially from the most downstream region of the experimental area where the beam dump was located. The geometrical characteristics of the TOF counters are listed in Table 2.3. All of the arrays were composed of vertical plastic scintillator bars.

Table 2.3: Configuration of the recoil arm scintillators.

	bar dimensions (w × h)	thickness	number of bars
RS1	65 mm × 220 mm	3 mm	6
RS2,3	200 mm × 1200 mm	30 mm	15
RS4	120 mm × 695 mm	10 mm	10

Since several elements of the RS1 array were located in the neutron beam, thin scintillators (3 mm,Bicron BC-404) and fast photomultipliers (Hamamatsu H2431) were selected. Elements of the RS2 and RS3 hodoscopes were modified from the neutron TOF counters used by the πAC group (KEK-PS E173, [24]).

All of the scintillators except the RS4 elements were instrumented with two photomultipliers at both top and bottom ends. These allowed the vertical hit position as well as the mean TOF to be determined. The TOF analysis is described in Chap. 3.

2.6 Trigger and Data Acquisition

Three kinds of triggers for the data acquisition system were prepared: (i) single-arm triggers used for inclusive measurements of charged particles, (ii) double-arm triggers used for exclusive measurements of γ and charged particles, and (iii) triggers for the neutron beam monitor. These triggers were applied in alternate beam spills in the ratio of (i):(ii):(iii) = 1 spill : 8 spills : 1 spill. For the measurement of the differential cross sections described in this paper, only the data from the single-arm triggers were used. The single-arm trigger was a prescaled sample of events with at least one hit in each of the scintillator arrays, RS1·RS2·RS3·RS4. The prescale factor was 400 for the 1 GeV runs and 99 for the 2 GeV runs.

Data were collected with a hybrid CAMAC and TKO [25] system, interfaced to a VAX 3500 computer. The computer was connected to a Kinetic Systems 3922 crate controller, which controlled the main CAMAC crate. The CAMAC MP's (memory-partner) on the main crate controlled the TKO-CH's and CAMAC-CH's. The TKO- and CAMAC-CH's handled the TKO and CAMAC crates respectively.

The data acquisition software was developed using the KEK-V buffering system made at KEK [26] on the computer. Event data were written on 8-mm tapes with an EXABYTE tape drive.

Data from each of the electronics modules (TDC, ADC, scaler etc.) for an event were stored in the MP modules. When the data stored in the MP's exceeded its maximum size (typically 5600 16-bit words), or when the spill end came, the data were transfered to the computer. The dead time of the acquisition system was monitored with scalers and the measured yields were corrected for these dead time losses. The dead time fraction of the single-arm trigger events was typically 59.06% for the full-target events of T_n = 1 GeV runs, 40.92% for the empty-target events of T_n = 1 GeV runs, 98.83% for the full-target events of T_n = 2 GeV runs and 97.12% for the empty-target events of T_n = 2 GeV runs.

The typical event size was about 300 16-bit words. The data acquisition system acquired about 100 events per second at maximum.

Chapter 3

Data Evaluation

3.1 Momentum Analysis

Particle momenta were determined from the measured hit positions in the wire chambers using a tracking algorithm based upon a Runge-Kutta method [27]. One (x,y) position for each chamber was deduced. Thus the tracking at 1 GeV was done with three x and y positions because PC2 was not available during 1 GeV runs, while at 2 GeV four positions were used. The tracking algorithm was applied to all combinations of hits on the chambers, and the track with the minimum χ^2 that passed through the target volume and had hits in the correct projected element of the RS2 array was selected.

Monte Carlo calculations were carried out to deduce the momentum resolution of the spectrometer. The Monte Carlo code included the position resolution of the chambers and multiple scattering by the materials (air, mylar window of chambers etc.). The particles generated at the hydrogen target with a certain momentum were tracked through the spectrometer system and the hit positions at the chambers were recorded. After these hit positions at the chambers were convoluted with their known position resolution, the randomized hit positions were analyzed with the same code used to analyze the experimental data. In Fig. 3.1, the difference between the generated and analyzed momenta is shown. The momentum resolution of the spectrometer was estimated to be, σ_p/p = 1.2% at p = 1 GeV/c, 2.2% at p = 2 GeV/c, and 3.1% at p = 3 GeV/c.

Figure 3.2 compares the momentum spectrum of the np $\rightarrow$ pn charge-exchange

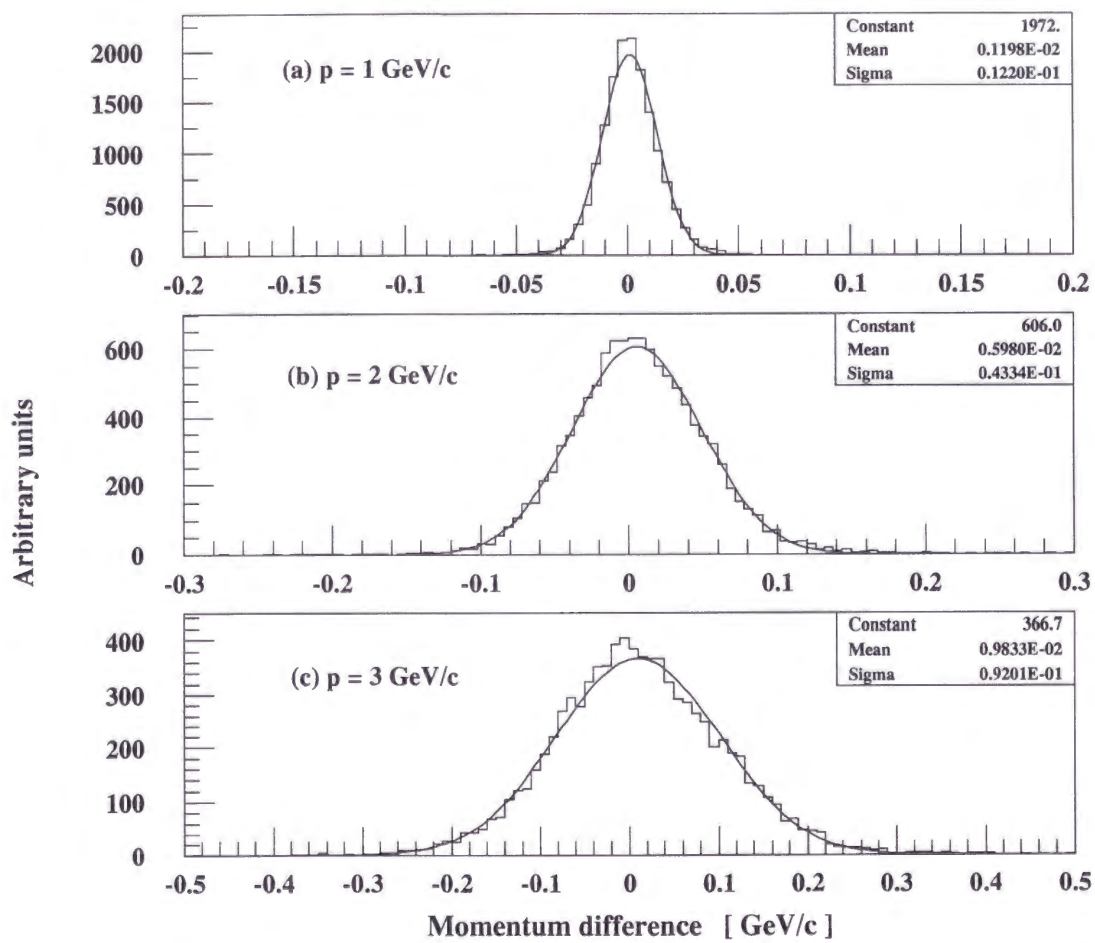

Figure 3.1: Difference between the Monte Carlo-generated momentum and the analyzed momentum from the analysis code.

peak at $\theta_{lab} = 6°$ and $T_n = 1$ GeV (the solid points in (a)) with a simple Monte Carlo result (the histogram in (b)). This Monte Carlo simulation includes the momentum spread of the neutron beam (7.2% in FWHM) and the momentum resolution (σ) of the spectrometer of 2.5%. The RMS width of the momentum distribution of the measured data is 78 MeV/c, while the simulated result is 79 MeV/c. Thus the momentum resolution from the Monte Carlo simulation (Fig. 3.1) and the momentum spread of the neutron beam quoted in Sec. 2.2 are consistent with the measured momentum spectra of the charge-exchange process.

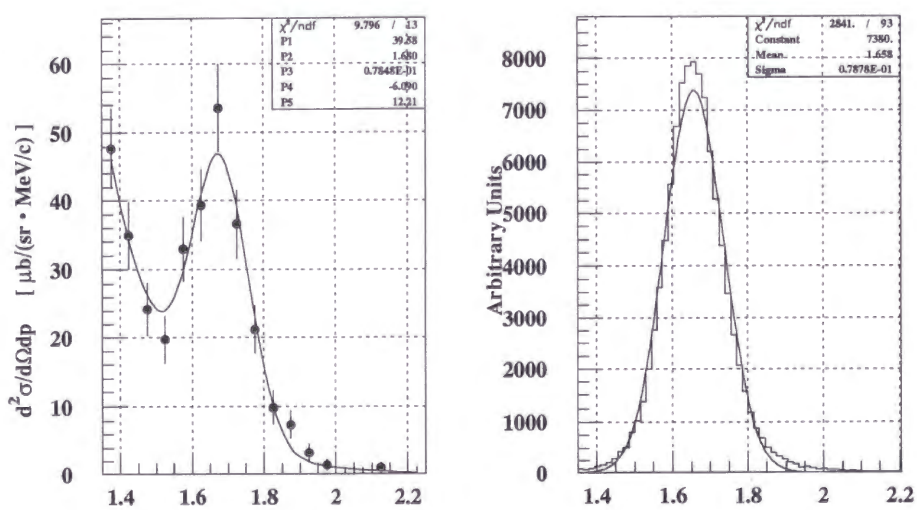

(a) charge exchange peak at 6 deg. **(b) MC result at 6 deg.**

Figure 3.2: Momentum spectra at $\theta_{lab} = 6°$ and $T_n = 1$ GeV: (a)Solid points are experimental data; (b)the histogram shows simple Monte Carlo simulation. The solid line in (a) shows the result of a fit to the data with a sum of Gaussian and exponential functions. The solid line in (b) shows a fit with a Gaussian function. P3 is the fitted value of the Gaussian σ.

3.2 Time-of-flight Evaluation

All of the scintillation counters used for the time-of-flight measurements were viewed by two photomultipliers. Signals from each tube were led to both ADC's and TDC's,

which allowed a slewing correction of the signal timing according to the measured pulse height.

The signal timing was dependent on the pulse height as shown in Figures 3.3(a) and (c). The corrected timing, t_c, was obtained using a following formula:

$$t_c = t + a + b/\sqrt{Q}, \tag{3.1}$$

where t is the measured timing from the TDC, Q was the pulse height from the ADC and a and b are the fitting parameters for each tube. An example of the corrected results is shown in Figures 3.3(b) and (d).

After this so-called slewing correction, the mean timing for each bar was obtained by averaging the corrected timings of the signals from two tubes at both ends.

Two photomultipliers at both ends of each bar allowed estimation of the vertical hit position of the scintillator from the time difference between both signals. The estimated hit position (y_{tdc}) was compared with that estimated from the track fitting (y_{track}) as shown in Fig. 3.4. The RMS width of the difference of these two for RS1 shown in Fig. 3.4(a) was typically 25 mm and that for RS2 shown in Fig. 3.4(c) was typically 30 mm. A cut at $\pm 3\sigma$'s on these figures was applied for the evaluation of the differential cross sections to reduce the accidental backgrounds.

Since the position resolution of the drift chambers was 320 μm, the main contribution to the RMS width of the difference of the two vertical positions was due to the timing errors. Thus the resolution of the timing measurement for each photomultiplier was estimated as 220 psec. and 100 psec. for RS1 and RS2 respectively. From these numbers the overall TOF resolution was estimated to be 350 psec.

The hit element of the scintillators predicted from the track fitting ($element_{track}$) was well correlated with the element which had valid TDC data ($element_{tdc}$). The element used for TOF calculation was selected so that $element_{track}$ should be the same as $element_{tdc}$ for RS1, and $element_{track}$ should be the same or adjacent to $element_{tdc}$ for RS2.

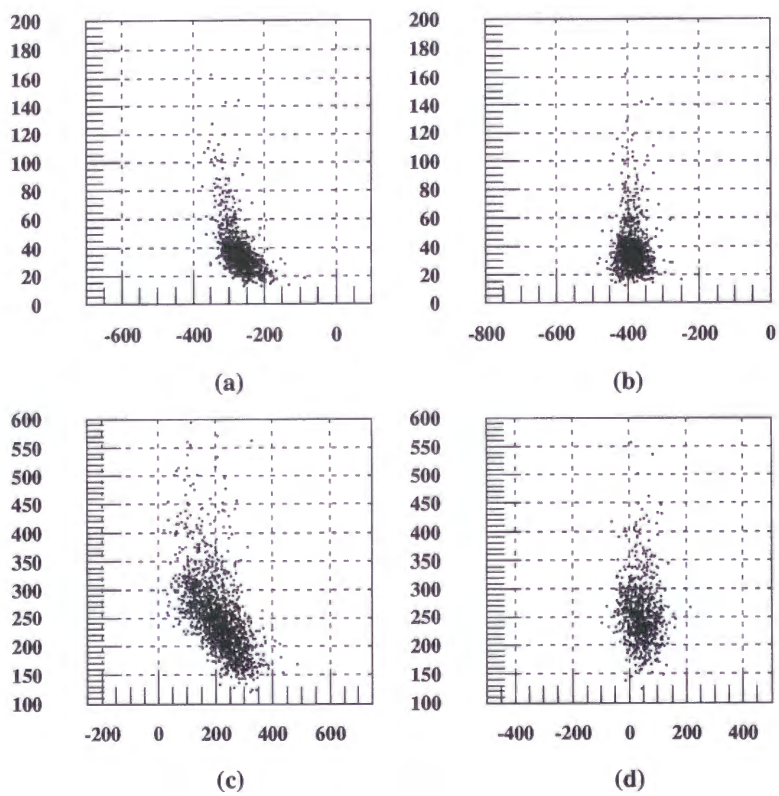

Figure 3.3: Two-dimensional plots of ADC channel (vertical) versus TDC channel (horizontal) for (a) an RS1 element before the slew correction; (b) an RS1 element after the slew correction; (c) an RS2 element before the slew correction, and (d) after the slew correction.

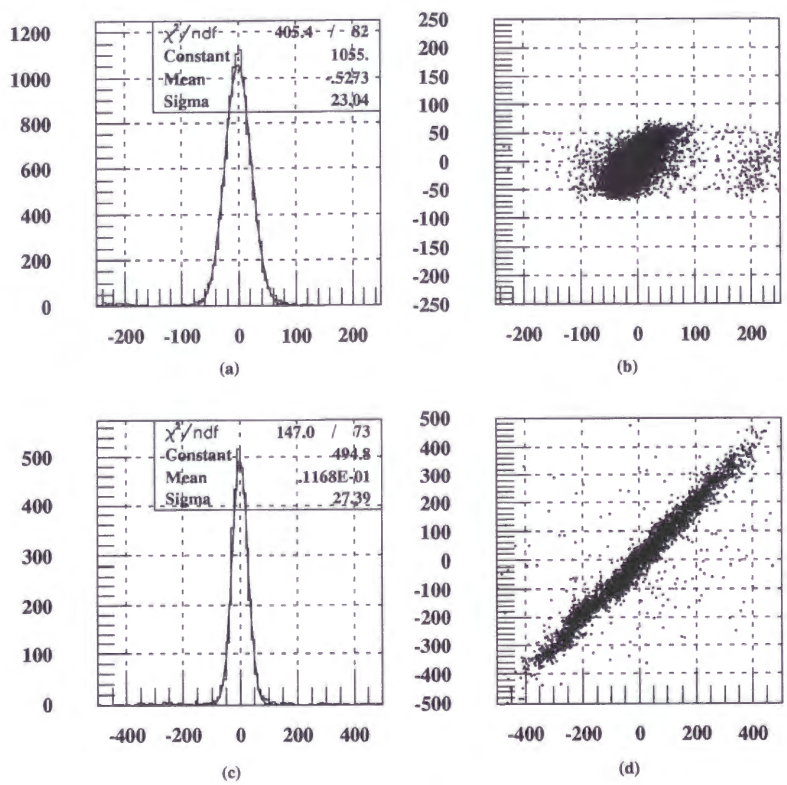

Figure 3.4: Comparison between the vertical position on an RS1 element ((a) and (b)) and on an RS2 element ((c) and (d)). (a) and (c) show $y_{track} - y_{tdc}$ as determined from the track fitting and from the relative timing of the two phototubes. Figures (b) and (d) show y_{track} (vertical) versus y_{tdc} (horizontal). Units are mm.

3.3 Particle Identification

The momentum determined from the track fitting procedure was combined with the particle velocity derived from the TOF measurement and the track length determined with the track fitting, in order to calculate the particle mass;

$$m = p\sqrt{1-\beta^2}/\beta, \tag{3.2}$$

where m is the particle mass, p is the particle momentum, and β is the velocity in the natural unit. Only protons and deuterons were observed since the spectrometer had no acceptance for low momentum pions.

The measured mass distributions at 1 and 2 GeV are shown in Fig. 3.5. It should be noted that these plot are the results of subtraction of target-full and target-empty runs. While the mass peaks for both protons and deuterons are sharp and well-defined, there remains a tail of the proton peak due to accidental hits on the RS1/RS2 hodoscopes. This is especially important for deuterons at $T_n = 2$ GeV (Fig. 3.6).

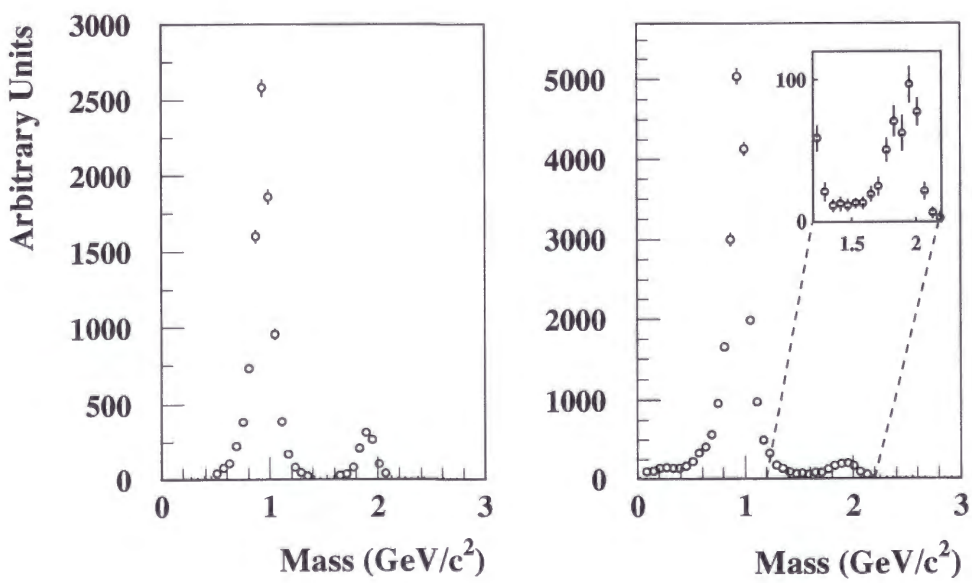

Figure 3.5: Recoil mass spectra for $T_n = 1$ GeV (left) and $T_n = 2$ GeV (right). The inset shows an expanded view of the deuteron peak at 2 GeV.

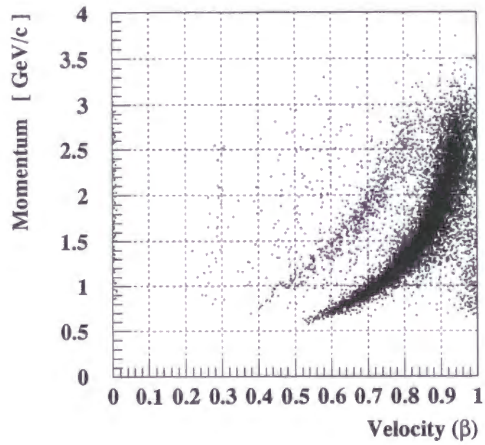

Figure 3.6: Momentum vs β at 2 GeV events. The two heavy bands correspond to recoil protons and deuterons.

In order to deduce the correction factors due to the proton tail, the proton peak in the mass spectrum was fitted with a Gaussian plus an exponential curve. The double-differential cross sections shown in Chapter 4 are corrected with these correction factors.

3.4 Background Subtraction

Target-empty events were used to subtract backgrounds from materials other than the liquid hydrogen target.

Figures 3.7(a)-(d) show the ratio momentum spectra for both full-target and empty-target events. The unfilled histograms are momentum spectra for full-target events, while the hatched areas show the empty-target events normalized to the full-target events according to the ratio of the SEC counts. The background subtraction was done with these normalized target-empty data.

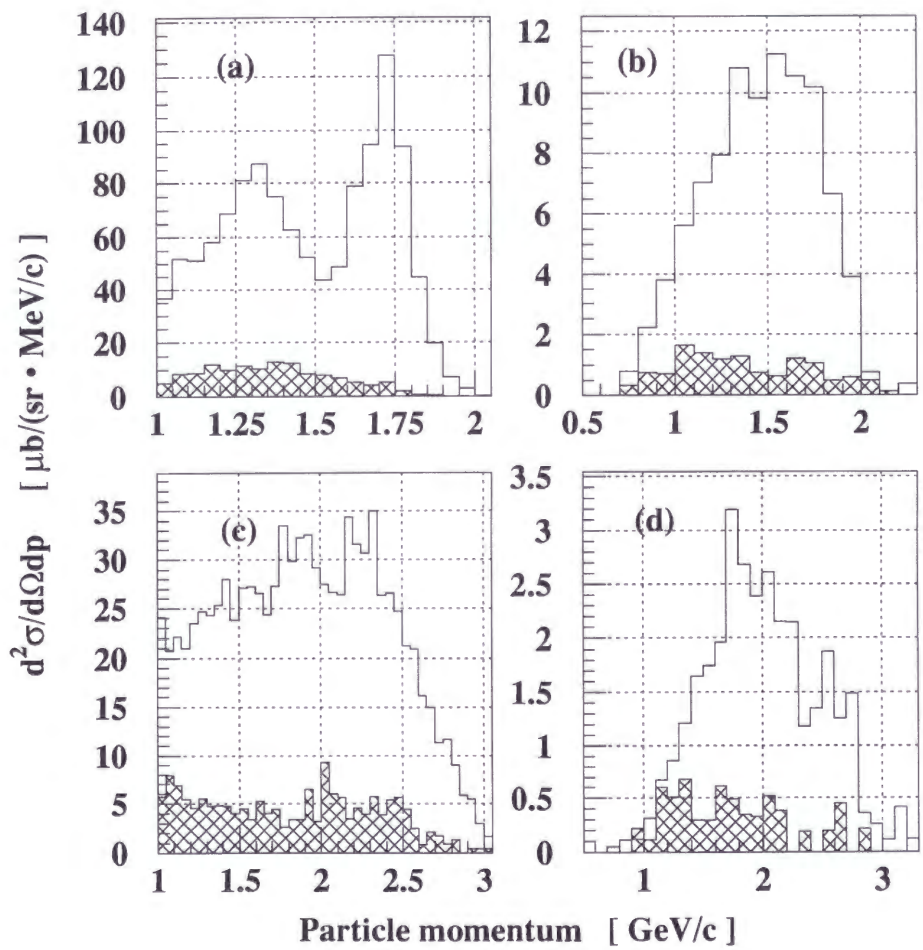

Figure 3.7: Double differential cross sections at $\theta^{lab} = 4°$ for full-target and empty-target runs. (a) protons at $T_n = 1$ GeV; (b) deuterons at $T_n = 1$ GeV deuterons; (c) protons at $T_n = 2$ GeV; and (d) deuterons at $T_n = 2$ GeV. The hatched areas show the spectra of the empty-target runs.

3.5 Evaluation of Cross Sections

The double-differential cross sections have been deduced from the usual expression,

$$\frac{d^2\sigma}{d\Omega dp} = \frac{Y}{\tau\ I\ P\ \eta_a\ \eta_c\ L\ \Delta\Omega\ \Delta p}, \tag{3.3}$$

where τ is the hydrogen target thickness, I is the number of incident neutrons, P is the trigger prescale fraction for data acquisition, η_a is the efficiency of the tracking and analysis procedure, η_c is the efficiency of the tracking chambers, L is the live time fraction of the acquisition computer and electronics, and $\Delta\Omega$ and Δp are the bin sizes for the solid angle and momentum.

Extensive Monte Carlo studies were done to determine the solid angle acceptance of the spectrometer as a function of both particle momentum and production angle (Fig. 3.8). These GEANT simulations considered the geometrical limitations imposed by the magnet as well as by each detector element.

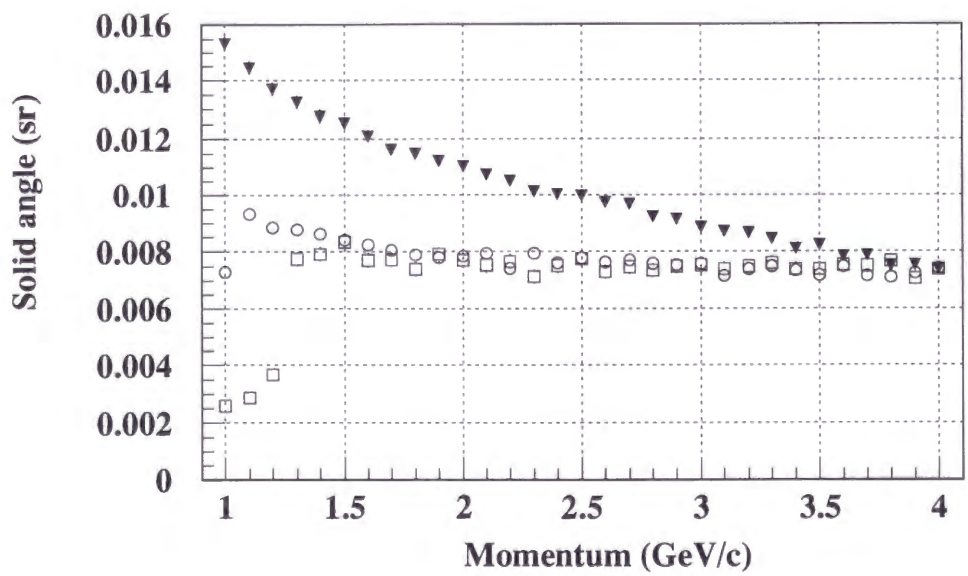

Figure 3.8: The Monte Carlo determined solid angle of the spectrometer for $\theta_{lab} = 5°$ (triangle), 10° (circle) and 15° (square). The theta bin width of 2° is used.

The analysis efficiency was similarly modeled with a Monte Carlo code which simulated the hardware trigger conditions and subjected events passing this requirement

to the same analysis package used to track and analyze the actual data. The measured position-dependent efficiency for each plane of the wire chambers was used as input to this simulation. The observed fraction of simulated hardware triggers which subsequently passed all tracking conditions determined the analysis efficiency.

The number of incident neutrons was deduced using the number of deuterons measured by the SEC.

3.6 Systematic Errors

The largest systematic uncertainty used to determine the cross sections was that due to the beam flux calculation. As was mentioned in Sec. 2.2, this uncertainty is estimated to be 27% at 1.0 and 2.0 GeV. When this is combined in quadrature with other considerably small uncertainties, the overall systematic uncertainty in the measured cross sections is estimated to be about 30%. The overall normalization is confirmed by the cross section of the charge-exchange process np $\rightarrow$ pn. At $T_n = 1$ GeV, the peaks of the charge-exchange process in the momentum spectra are clearly identified, and the cross sections agree well with each other within the systematic uncertainty of 30% as shown in Sec. 4.1. At $T_n = 2$ GeV, although the peaks of the charge-exchange process are not clear, the measured proton yields are consistent with the estimation from the previous data described in Sec. 4.1. Furthermore, the rate dependence of the normalization has been checked. The measured proton yields above 2 GeV/c normalized with SEC counts per spill are compared between high- and low-counting rate runs. The SEC counts per spill for the high-counting rate runs was 469 and that for the low-counting rate run was 393, and the normalized proton yields for the high- and low-counting rate runs are in agreement well within the statistical uncertainties of 3%.

Chapter 4

Results and Discussion

4.1 Cross Sections for the Charge-exchange Process

Proton emission at forward angles is dominated by the charge-exchange reaction and has been previously measured. Earlier data near our energy [28, 29, 30, 31] indicate that the forward-angle cross section multiplied by $p_{n,lab}^2$ is approximately independent of energy, as shown in Fig. 4.1(a) [28]. This fact implies that the helicity amplitudes are roughly independent on the total energy s. However there may be systematic normalization differences between these data. Mischke *et al.* [29] stated that the uncertainties in the absolute normalization of their data (0.6 to 2 GeV/c) were 3 to 10%. According to Miller *et al.* [30], the estimated absolute systematic uncertainty in their data (3 to 12 GeV/c) was ±20%. Bizard *et al.* [28] stated that the systematic error on the absolute normalization of the incident neutron flux was ±5%. At small momentum transfer, the differential cross section $d\sigma/dt$ is found to depend only on the momentum transfer t, falling exponentially at increasing |t| (Fig. 4.1(b)). At T_n = 1 GeV (p_n = 1.7 GeV/c), the differential cross section $d\sigma/dt$ for -t > 0.01 $(GeV/c)^2$ can be fitted with the function

$$\frac{d\sigma}{dt} = \frac{130}{p_{lab}^2}(-0.34 \log|t| - 0.12). \tag{4.1}$$

At T_n = 2 GeV (p_n = 2.8 GeV/c), we find

$$\frac{d\sigma}{dt} = \frac{110}{p_{lab}^2}(-0.34 \log|t| - 0.12). \tag{4.2}$$

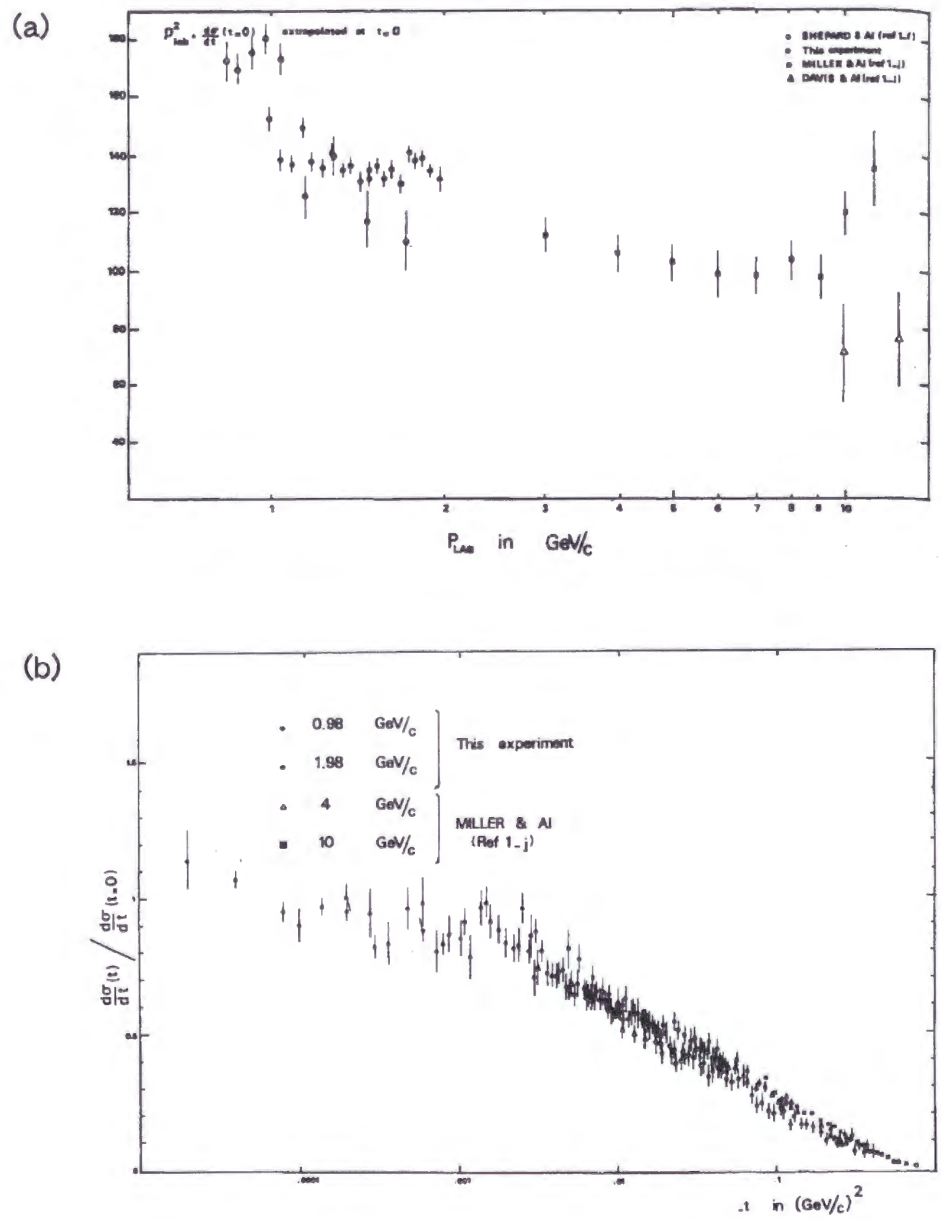

Figure 4.1: Systematics of the charge-exchange reaction np $\rightarrow$ pn by G. Bizard *et al.*: (a) $P_{lab}^2 d\sigma(t = 0)/dt$ versus P_{lab}; (b) $(d\sigma(t)/dt)/(d\sigma(0)/dt)$ versus the momentum transfer squared for various incident momenta: 0.98, 1.98, 4, and 10 GeV/c.

It should be noted that this asymptotic function may have the normalization uncertainty of about ±20% due to the uncertainties of previous data.

A typical proton momentum spectrum at 1 GeV and $\theta^{lab} = 4°$ obtained in this experiment is shown in Fig. 4.2. It is noted that the background subtraction using the target-empty runs was made for this spectrum and for all of the results shown in this chapter. The errors shown in these spectra reflect only statistical uncertainties. The prominent peak near 1.7 GeV/c is due to the charge-exchange reaction, while the broader peak centered near 1.3 GeV/c results from excitation of the Δ resonance.

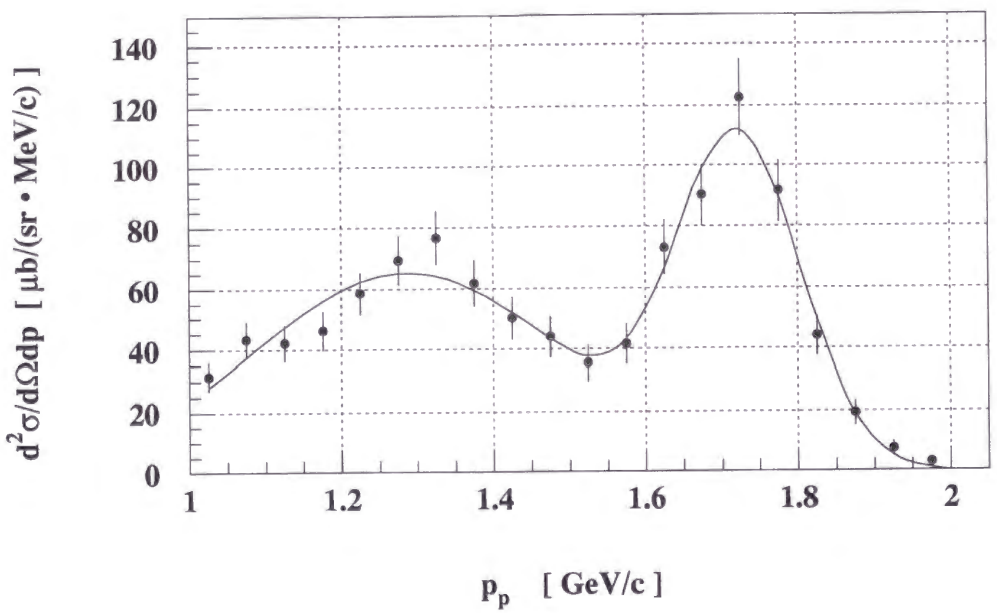

Figure 4.2: The double-differential cross sections for np → pX at 1 GeV for θ_{lab} = 3-5°.

The charge-exchange peak was fitted with a Gaussian function along with the Δ peak as shown by a solid line in Fig. 4.2. With the fitting, the differential cross sections $d\sigma/d\Omega$ of the charge-exchange process, np → pn, at T_n = 1 GeV were obtained, and are shown as the open circles in Fig. 4.3. The solid line shown the trend of the previous data, and was obtained directly from eq. 4.1. Although the differential cross sections at θ^{lab} = 6°, 8° and 10° are lower than the previous data (eq. 4.1), their disagreement is generally within the systematic uncertainties of 30% quoted in Sec.

3.6.

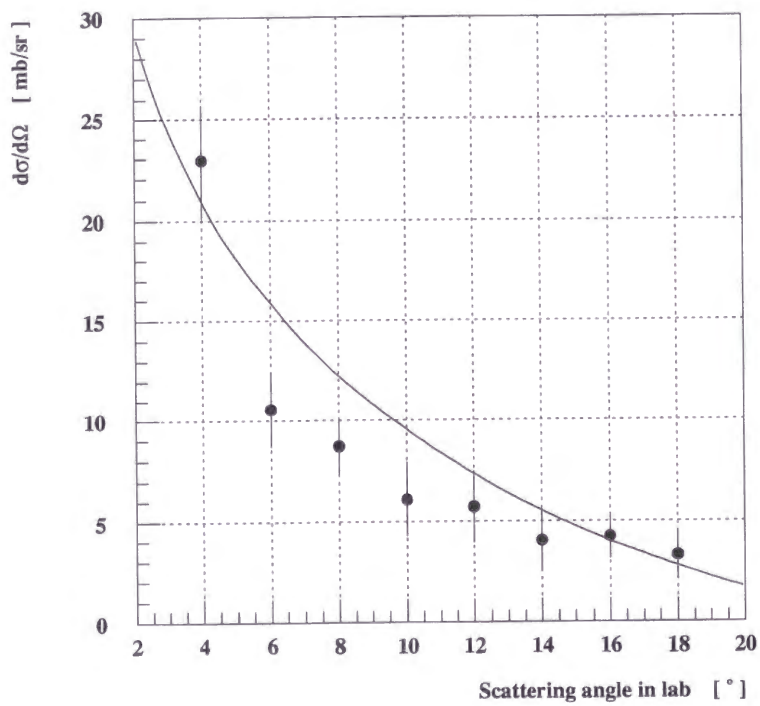

Figure 4.3: Comparison of the present cross sections for the charge-exchange reaction at $T_n = 1$ GeV (solid circles) with the estimation from the previous data (solid curve). See text on the treatment of the previous data.

Because the charge-exchange peaks are not seen in our proton momentum spectra at $T_n = 2$ GeV, the estimated yields from the previous data (eq. 4.2) are compared with the measured spectra. The estimated charge-exchange peak is determined from the previous data and known momentum resolutions of our spectrometer and neutron beam. The estimated peak is consistent with the measured momentum spectra within the quoted systematic uncertainties of 30% for our data and 20% for the previous data.

In summary of this section, the overall normalization used to evaluate the double-differential cross sections agree with the systematics of the previous charge-exchange data within the quoted uncertainties.

4.2 Double Differential Cross Sections for np → dX

In this section, the measured momentum spectra ($d^2\sigma/d\Omega dp$) are shown. All the error bars shown in this section contain only the statistical uncertainties. It should be noted that the results at $T_n = 2$ GeV are the highest energy data with a narrow-band neutron beam and a magnetic spectrometer of wide acceptance.

4.2.1 $d^2\sigma/d\Omega dp$ at $T_n = 1$ GeV

Our measured deuteron momentum spectra at laboratory angles ranging from 4° to 12° are shown in Fig. 4.4 for an incident neutron energy of 1 GeV. The solid curves show the result of a calculation by the one-nucleon-exchange model for np → d$\pi\pi$ process through a σ meson (Fig. 4.5(a) [8]). Similar data have been obtained at T_n = 0.8 GeV [7] and 1.2 GeV [3]. Our measured momentum spectra qualitatively agree with the 0.8 GeV results. The momentum spectrum at $\theta_d^{lab} = 1.5°$ at $T_n = 1.2$ GeV has sharp peaks near the two-pion threshold and a remarkable bump in the highest missing mass region. The authors of [3, 4] assigned the bump in the highest missing mass region as the contribution from np → dη process. The spectra of other angles at $T_n = 1.2$ GeV also have peaks near the two-pion threshold. The peaks near the two-pion threshold of the present results are not so clear as the measured spectra of $T_n = 1.2$ GeV [3], and it would be due to the difference of the energy.

4.2.2 $d^2\sigma/d\Omega dp$ at $T_n = 2$ GeV

The difference between our results and the model calculation might be attributable to the contribution of other reaction mechanisms. For example, excitation of a $\Delta\Delta$ intermediate state (Fig. 4.5(b)) was previously found to be important at $T_n = 1.2$ GeV [14, 8].

The measured deuteron yield at momenta both above and below the kinematic limits for two-pion production is due to the reaction np → dπ^0. The isospin-related process pp → dπ^+ has been previously measured at this energy [32]. Our new np results are found to be consistent with the pp data.

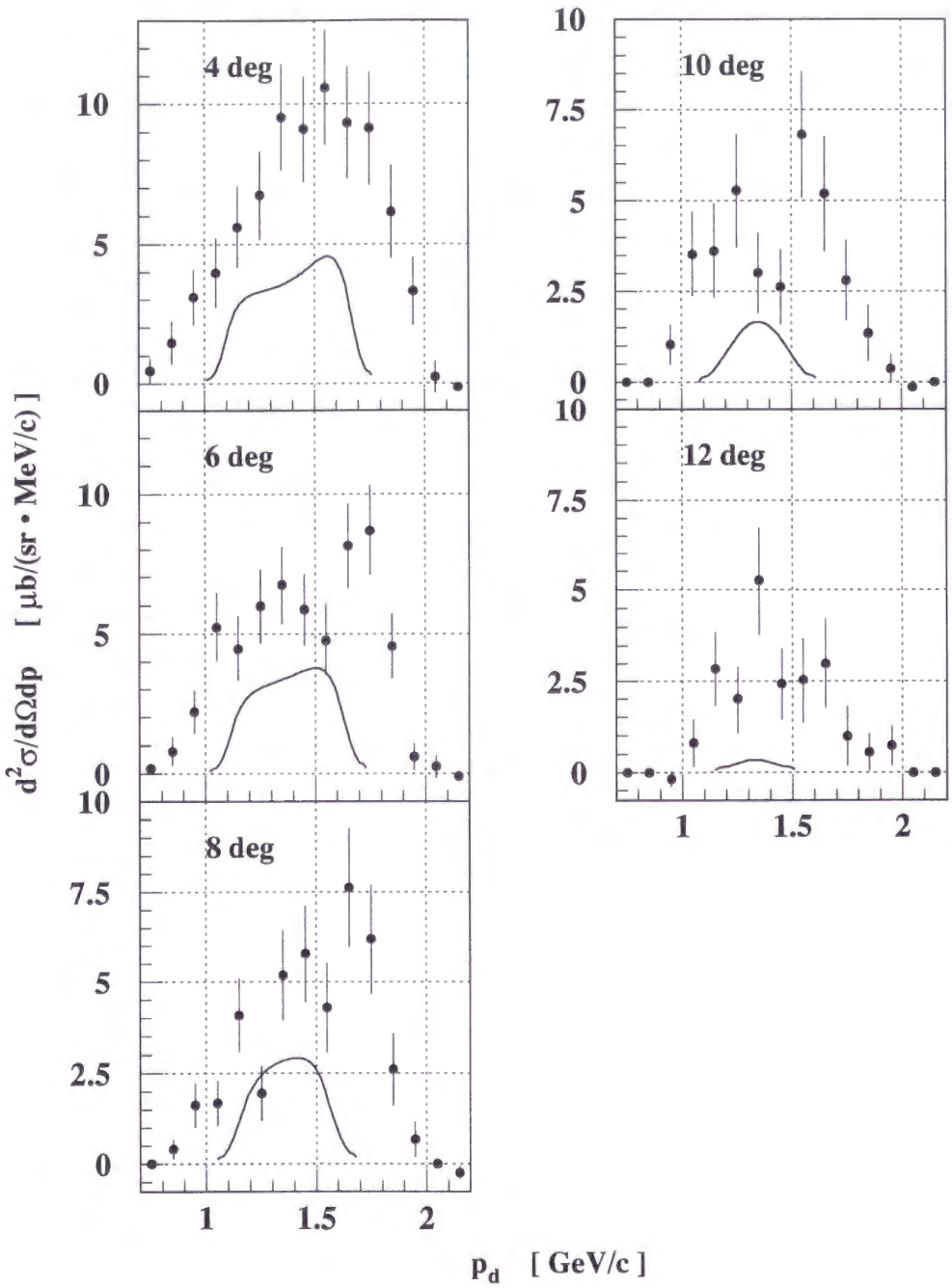

Figure 4.4: The double-differential cross sections in the lab frame for np → dX at T_n = 1 GeV. The solid lines show the results of the theoretical calculation of the one-nucleon-exchange model. They also indicate the only regions where two-pion production is kinematically allowed. The calculated results are not convoluted with the momentum resolutions of the neutron beam and the spectrometer.

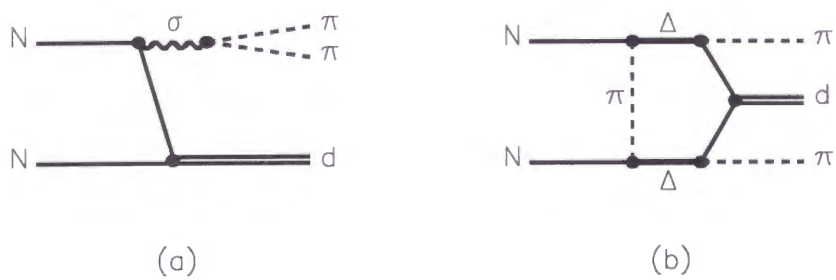

Figure 4.5: Diagrams of the theoretical models: (a) the one-nucleon-exchange model; (b) the $\Delta\Delta$ model.

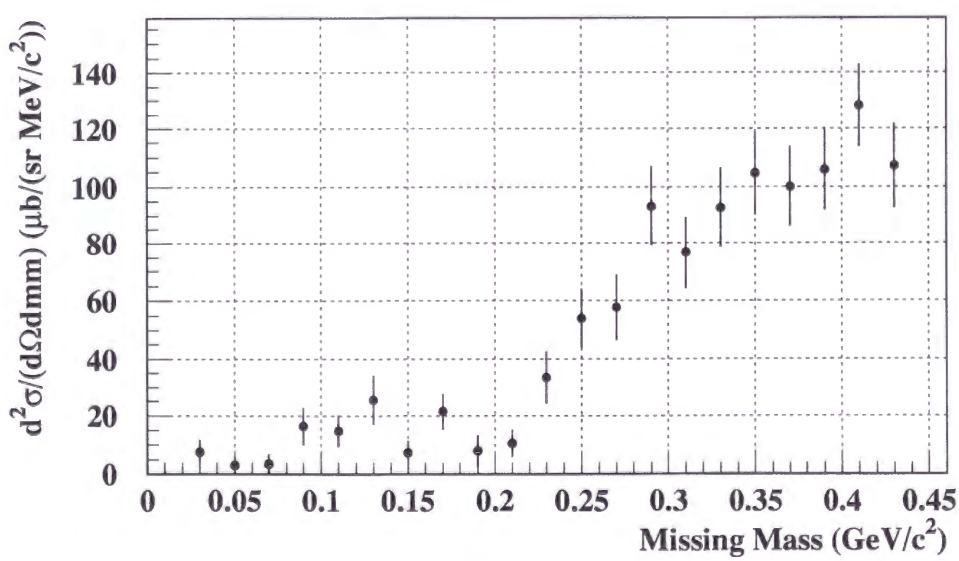

Figure 4.6: Missing mass spectrum for the reaction np $\rightarrow$ dX at θ_{lab} = 3°-13° and T_n = 1 GeV.

The missing mass spectrum for deuteron lab. angles from 3° to 13° is shown in Fig. 4.6. Single-pion production produces a rather broad peak around 140 MeV, whereas in the region of the two-pion threshold the yield is observed to be rapidly increasing. This result confirms the fact that the contribution of two-pion production is dominant in this energy.

The deuteron momentum spectra for an incident energy of 2 GeV have been measured for the first time, and the spectra at laboratory angles ranging from 4° to 14° are shown in Fig. 4.7. The solid curves are the results of the theoretical calculation with the one-nucleon-exchange model described in detail in Sec. 4.3.

The measured distributions are seen to be qualitatively different from the 1 GeV results, signaling the presence of additional reaction mechanisms at this higher energy. In particular, at angles less than 12° there is an observed suppression of the yield near the two-pion production peaks relative to an enhanced deuteron yield near 2 GeV/c. At these angles the one-nucleon-exchange model compares poorly with the data. As in the case at 1 GeV, the deuteron yield at the highest and lowest momenta measured - in the kinematic region below two-pion threshold - are found to compare favorably with previous single-pion production data in pp scattering near this energy [33].

The sources of the additional structure around the center of the measured momentum distribution (i.e. in the largest missing mass region) are evident in the missing mass spectrum shown in Fig. 4.8. These results have been generated from deuteron events emitted in the angular range from 3° to 9°. Dominating this distribution are two broad peaks centered at the η and ρ masses. While the beam energy is well above the threshold for η production, the full width of the ρ peaks is not observed and has been cut off in this figure.

The solid and dashed lines are the results of Monte Carlo simulations of the reactions $np \rightarrow d\eta$ and $np \rightarrow d\rho$ which include the momentum spread of the neutron beam and the momentum resolution of the spectrometer. The normalizations are arbitrary. The simulations show the expected reconstructed η and ρ missing mass distributions, if they exist.

The missing mass distribution and the Monte Carlo simulation suggest that the contribution of $np \rightarrow d\eta$ and $np \rightarrow d\rho$ reactions should be considered in order to

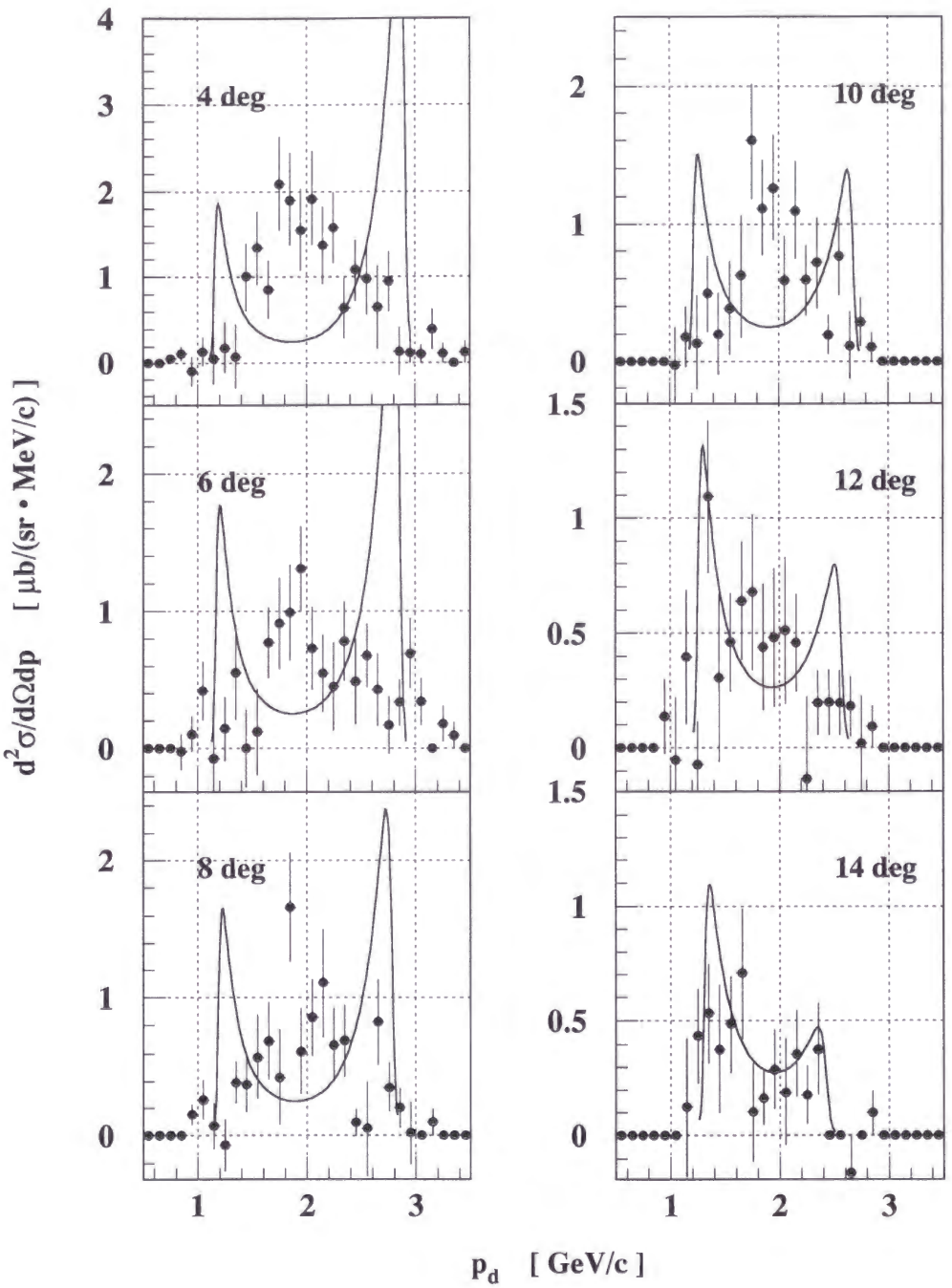

Figure 4.7: The double-differential cross section in the lab frame for np → dX at T_n = 2 GeV. The solid lines give the results of the theoretical calculation in the one-nucleon-exchange model. These curves also indicate the only regions where two-pion production is kinematically allowed. The calculated results are not convoluted with the momentum resolution of the neutron beam and the spectrometer.

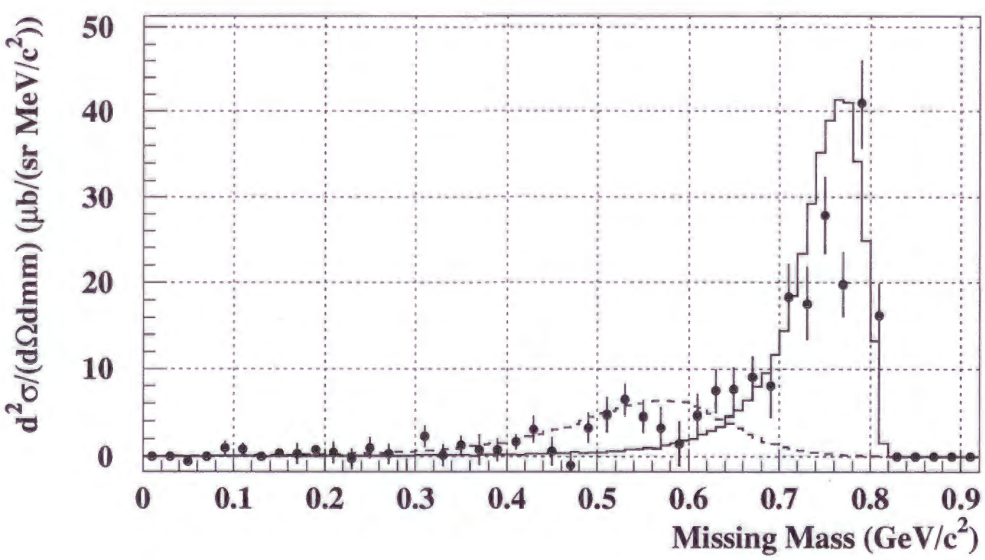

Figure 4.8: Missing mass spectrum for the reaction np $\rightarrow$ dX at θ_{lab} = 3°-9°, T_n = 2 GeV. The solid line is a result of Monte Carlo simulation for the np $\rightarrow$ dρ reaction, and the dashed line is for the np $\rightarrow$ dη reaction. Details are given in the text.

describe the np → dX reaction in this energy region.

4.3 Comparison with the One-nucleon-exchange Model

Yoshino *et al.* [8] calculated the momentum spectrum of np → dX reaction according to the one-nucleon-exchange model. The diagrams of this model are shown in Fig. 4.9(a)(b).

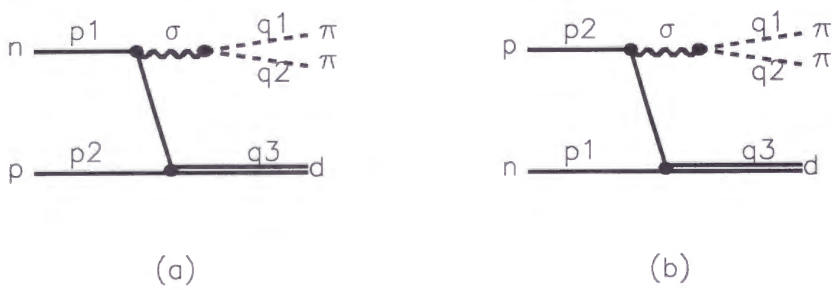

Figure 4.9: Diagrams of the one-nucleon-exchange model: (a) t-channel (forward), (b) u-channel (backward).

In their calculation, the scattering amplitudes are assumed to be a product of the Born amplitudes of $np \to \sigma d$ (F^B) and the decay amplitudes of $\sigma \to d(\pi\pi)^0$ (F^d):

$$\mathcal{F}_{\lambda\mu_1\mu_2} = F^B_{\lambda\mu_1\mu_2} \cdot F^d(s_{12}). \tag{4.3}$$

Here λ, μ_1 and μ_2 are the helicities of the deuteron, neutron, and proton, respectively. The variables in the amplitudes are the Lorentz invariants defined by $s = (p_1 + p_2)^2$, $s_{12} = (q_1 + q_2)^2$, $t3 = (p_1 - q_3)^2$ and $u_3 = (p_2 - q_3)^2$, where p_1 and p_2 are the 4-momentum of the neutron and the proton respectively, q_3 is the 4-momentum of the deuteron and q_1 and q_2 are the 4-momenta of pions. The decay amplitudes $F^d(s_{12})$

are calculated from the I=0 s-wave $\pi\pi$ phase shift ($\delta_{\pi\pi}$) as,

$$F^d(s_{12}) = \frac{1}{q^*(s_{12})} exp(i\delta_{\pi\pi}(s_{12})) \sin\delta_{\pi\pi}(s_{12}), \tag{4.4}$$

where $q^*(s_{12})$ is the magnitude of the pion momentum in the pion rest frame. The formalism of this model including F^B is described in detail in Appendix A.

In Figures 4.4 and 4.7, the results of this calculation are shown. At T_n = 1 GeV, the calculated results underestimate the measured spectra. Especially at 4° and 6°, the bumps in the calculated spectra near the kinematic threshold for two-pion production are the signature of the ABC effect. The ABC effect is the excess near the two-pion threshold in I=0 channel [5], and believed to be related with the reaction mechanism as mentioned in Chapter 1. At T_n = 2 GeV, the calculated spectra show sharp ABC peaks, whereas the measured spectra do not have such peaks. Furthermore, the calculation do not reproduce the bumps in the highest missing mass region, which are suggested to be the contribution of the np $\rightarrow$ dρ process in Sec. 4.2.2.

As is seen from eq. A.8, the ABC peaks, the cross section enhancements near the two-pion thresholds (both high- and low-p_d regions) are produced by nucleon pole singularities, especially at T_n = 2 GeV in the one-nucleon-exchange model. In the intermediate region (i.e. at large missing mass region), the calculated spectra are affected by the interference of the t- (forward) and u- (backward) channel.

As the authors of ref. [8] used in their paper, the value of the coupling constant $g_{\sigma NN}$ = 0.82 is used and the s-wave phase shift of Case B in [8] is applied. These parameters were determined by a fit to the momentum spectra at p_n = 1.46 GeV/c (T_n = 0.797 GeV [7]) and p_n = 1.9 GeV/c (T_n = 1.18 GeV [3]). Since these parameters strongly affect the calculated results, each of them is discussed individually below.

Coupling constant In the theory of free nucleon-nucleon interaction, the coupling constant at the σNN vertex is normally taken as $g^2_{\sigma NN}/4\pi \sim 5.7$ [34], thus $g_{\sigma NN} \sim$ 8.46. Yoshino *et al.* [8] used the value of the coupling constant about 10 times smaller than this value, while they did not mention the reason why the coupling constant is so small. Some missing mechanism which cancels the amplitudes might exist. It

should be noted that Yoshino *et al.* did not use a form factor at the σNN vertex (see eq. A.8). If the form factor is included in the calculation, the resultant differential cross section will be reduced to 1/2 or 1/3 at $T_n = 2$ GeV. At $T_n = 1$ GeV, the results will not change much if the form factor is included.

$\pi\pi$ phase shift Because the differential cross section is proportional to $\sin^2 \delta_{\pi\pi}(s_{12})$, the shape of the momentum spectrum strongly depends on the behavior of the phase shift $\delta_{\pi\pi}$ and the momentum dependence of $\sqrt{s_{12}}$. The momentum dependence of $\sqrt{s_{12}}$ is shown in Fig. 4.10.

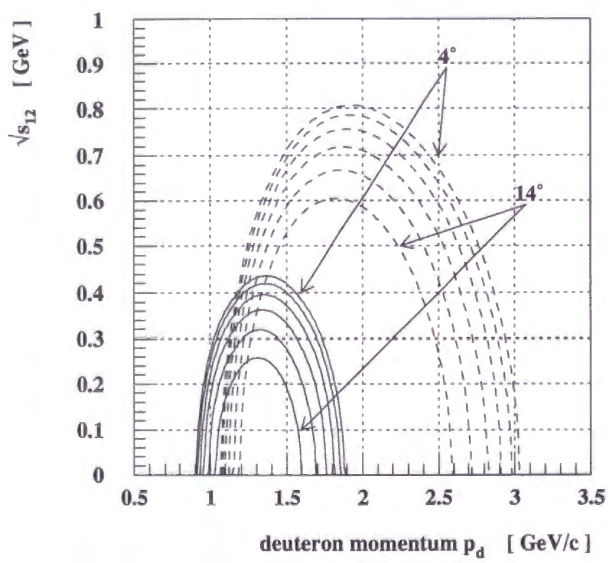

Figure 4.10: Deuteron momentum dependence (p_d) of the missing energy for inclusive deuteron production via np $\rightarrow$ dX. The solid lines are for $T_n = 1$ GeV, and the dashed lines are for $T_n = 2$ GeV. The curves show the kinematics for $\theta_d^{lab} = 4°$-$14°$ in 2° steps.

The I=0 s-wave $\pi\pi$ phase shift below $\sqrt{s_{12}} < 0.55$ GeV is shown in Fig. 4.11. The phase shift has been determined by the reaction π^-p $\rightarrow \pi^+\pi^-$n [12] and $K^+ \rightarrow \pi^+\pi^- e^+\nu$ decay [10, 11]. Unfortunately, because the experimental data for the low energy $\pi\pi$ phase shift below $M_{\pi\pi}$ $(= \sqrt{s_{12}}) = 0.5$ GeV are not sparse, there is room for Yoshino *et al.* or others to adjust the phase shift. Because the phase shift of $M_{\pi\pi}$

$\sim$ 0.5-0.8 GeV affects the cross sections at T_n = 2 GeV and the value larger than the results of the fitting by Froggatt *et al.* [12] is used for the theoretical calculation, the calculated differential cross section at T_n = 2 GeV will be smaller if the phase shift is adjusted to lower value. In this case, the difference between the theoretical calculation and the data in Fig. 4.7 becomes smaller.

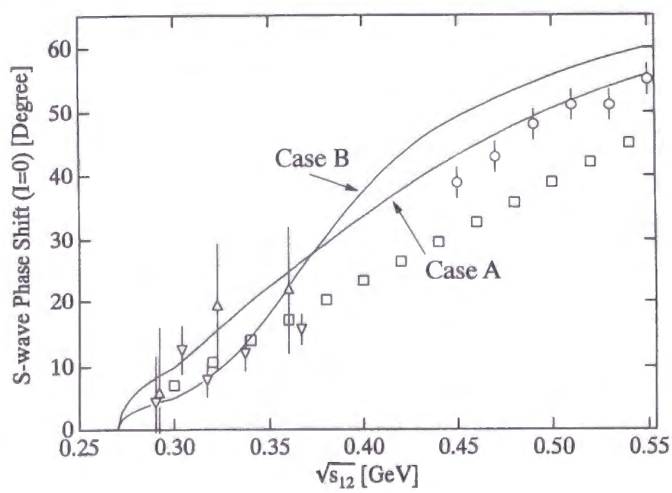

Figure 4.11: I=0 s-wave $\pi\pi$ phase shift below 0.55 GeV. The horizontal axis is the invariant mass of the two-pion system. Case B is used in the calculation of the one-nucleon-exchange model. The phase shifts shown by the symbols ○, □, ▽, and △ are those of Grayer *et al.*, Froggatt *et al.*, Rosselet *et al.*, and Zylbersztein *et al.*, respectively. The phase shifts shown by □ are not an experimental result, but a result of a fitting using the measured data of $M_{\pi\pi} > 0.6$ GeV and Rosselet *et al.*

A theoretical calculation of the np $\rightarrow$ dρ process is in progress by K. Tamura and the present author. This process should be independent of the np $\rightarrow$ dσ process. In other words, the differential cross section is the sum of the contribution of the np $\rightarrow$ dρ process and that of the np $\rightarrow$ dσ process and there is no interference between these two, because their partial waves of the π production are different from each other. This calculation might explain the bump in the largest missing mass region at T_n = 2 GeV.

4.4 Summary of Discussion

Our measured deuteron spectra have been compared with the theoretical calculation based on the one-nucleon-exchange model. At $T_n = 1$ GeV, the theoretical calculation underestimates the measured spectra. Other processes, like the $\Delta\Delta$ intermediate state, should be considered at this energy. The measured missing mass spectrum indicates a rather broad peak around the pion mass and an important contribution of the two-pion production. At $T_n = 2$ GeV, the measured spectra do not have sharp ABC peaks near the two-pion threshold, whereas the one-nucleon-exchange model expects them and overestimates the double-differential cross sections around these peaks. The possible reasons for this poor agreement around the ABC peaks are: (i) the I=0 s-wave $\pi\pi$ phase shift used for the calculation is not appropriate, (ii) the coupling constant $g_{\sigma NN}$ is still too large, and (iii) the form factor at the σNN coupling is not included. The missing mass spectrum at this energy suggests the large role played by the $np \rightarrow d\eta$ and $np \rightarrow d\rho$ processes. In order to clarify the reaction mechanism at a few GeV, further theoretical work including the calculation on the $np \rightarrow d\rho$ process is needed.

Chapter 5

Conclusion

The double-differential cross sections ($d^2\sigma/d\Omega dp$) have been measured for the np $\rightarrow$ dX reaction at the neutron beam energies of 1.0 GeV and 2.0 GeV. The data at T_n = 2 GeV are the first results in this energy region. The methods used by this experiment have been shown. A neutron beam line was newly constructed at KEK-PS for this experiment, and this provides the highest energy neutron beam in the world. The quasi-monoenergetic neutron beam was made from breakup reaction of deuterons extracted from the KEK-PS. Typically 1×10^8 neutrons per sec. of 1 GeV and 2 GeV were used.

Protons and deuterons from neutron-proton reactions were tracked by a magnetic spectrometer to determine their momenta and the time-of-flight was measured. Then the deuteron momentum spectra at θ_d^{lab} = 4°, 6°, 8°, 10°, and 12° for T_n = 1 GeV were obtained. The theoretical calculation based on the one-nucleon-exchange model (two-pion production through a σ meson) underestimates the double-differential cross sections. The present results are consistent with the similar measurement at T_n = 1.2 GeV [3] and suggest that the mechanisms other than the one-nucleon-exchange model should be taken into account. The missing mass spectrum for T_n = 1 GeV implies that the two π production processes are dominant in the np $\rightarrow$ dX reaction in this energy and the two π interactions at the invariant mass below 0.5 GeV should be investigated more precisely.

At T_n = 2 GeV, the deuteron momentum spectra at θ_d^{lab} = 4°, 6°, 8°, 10°, 12°, and 14° were obtained. The measured momentum spectra do not show remarkable peaks near the two-pion threshold which were called as the ABC peaks. However

the measured spectra show a bump in the highest missing mass region. They were also compared with the calculation of the one-nucleon-exchange model which expects sharp ABC peaks. The measured bumps in the highest missing mass region exceed the theoretical calculation. The missing mass spectrum suggests that especially ρ production plays an important role in the np $\rightarrow$ dX reaction along with η production. This is the first data at this energy for the np $\rightarrow$ dX reaction and further experimental and theoretical work will deepen our understanding on the mechanism of the nucleon-nucleon reaction in this energy region.

Acknowledgements

First of all, I would like to express my sincere thanks to all the collaborator of the present experiment (KEK-PS E235) for their efforts to accomplish the experiment; Prof. T. Hasegawa, Prof. N. Horikawa, Dr. S. Ishimoto, Dr. T. Iwata, Dr. Y. D. Kim, Mr. M. Kawabata, Prof. M. A. Kovash, Prof. Y. Mizuno, Mr. F. Nakayama, Mr. H. Ogami, Mr. A. Ogawa, Mr. T. Sasaki, Prof. T. -A. Shibata, Dr. K. Tamura and Mr. J. Trice. Prof. Michael A. Kovash is the spokesperson of the experiment and I have had continuous discussion with him during all the stages of the experiment - the preparation of the experimental apparatus, the beam time and the analysis. He has always encouraged me and he also supported me financially. Prof. Toshi-Aki Shibata has worked with me as a key person living in Japan. I am strongly indebted to Dr. Keisuke Tamura for many useful discussions and suggestions on the theoretical aspects.

I deeply appreciate the encouragement, advice and discussion of my supervisor of the graduate study, Prof. Kenichi Imai. Although he is not a member of the present experiment, I am strongly indebted to him to complete this thesis.

I am grateful to Prof. Akira Masaike for the encouragement and instructions throughout my graduate study. The variety of his interest not only in nuclear and particle physics but also in other regions of physics affected me strongly.

I thank Prof. Hideto En'yo very much for many advices on the preparation and the analysis of the experiment based on his various experience in many laboratories in the world. His encouragement and discussion with him throughout the graduate study were very worthwhile.

This experiment was made available by the successful acceleration of deuterons at KEK-PS. Many efforts made by the members of the accelerator division should be

appreciated. Especially I thank Prof. Motohiro Kihara and Prof. Yoshiharu Mori for their leadership on the project of the deuteron acceleration. Prof. Yoshiharu Mori also supported me at INS, University of Tokyo in the last year of the graduate study.

I thank Prof. Koji Nakai, who was the director of the PS division of the National Laboratory for High Energy Physics (KEK), for his continuous encouragement throughout the experiment. I also thank Prof. Junsei Chiba for his arrangement for many kinds of our requests. In addition he was the spokesperson of the APEX experiment held at KEK-PS and his leading to enjoy physics is admired.

The newly constructed neutron beam line was a result of the collaboration with Prof. Minoru Takasaki, Prof. Kazuhiro Tanaka, Dr. Hiroyuki Noumi and other members of the beam-channel group of KEK-PS. Especially I am deeply indebted to the efforts in the design and construction of the beam line of Dr. Hiroyuki Noumi. I also thank the members of other supporting group of KEK-PS whose support in various aspects such as electronics or data acquisition was indispensable for the experiment.

I would like to express my special thanks to Prof. Noboru Hiroshige and Prof. Tamotsu Ueda for providing the theoretical calculation of the one-nucleon-exchange model. Discussion on the theoretical aspects of this work with them is also acknowledged.

I express my sincere gratitude to Dr. Satoru Yamashita. He provided me the core part of the Runge-Kutta code. In addition, he has been a very good friend since my graduate study started as other colleagues, Dr. Naohito Saito, Dr. Yuji Goto, Dr. Hidetoshi Akimune and Mr. Shuichi Kuwamoto. We started our graduate study at the same time about 8 years ago. Since then we have enjoyed many discussions on physics and strongly affected each other. I believe we will extend the frontier of the fantastic world of physics on the basis of the days in the graduate school.

I thank Prof. Shinsaku Kobayashi, Prof. Harutaka Sakaguchi, Dr. Masanobu Nakamura, Dr. Kiyohiko Takimoto, Dr. Tetsuya Murakami, Mr. Masaru Yosoi and other members of the NE (experimental nuclear physics) group, to which I belong during the graduate study, for their countless encouragement, discussion and collaboration. The NE group is my birth place as a physicist and I have grown up in the vivid and energetic atmosphere of the NE group. Especially Dr. Tetsuya Murakami was an

adviser of my master's work on the high energy gamma rays and I am indebted to him for his instructions and advice on everything in detail.

I would like to thank Ms. Eiko Takahashi and Ms. Keiko Nakagawa for their thorough administration work. Because I spent many days at KEK and the sites other than Kyoto University, their complete work was indispensable. I am grateful to Ms. Yuka Nakakoji for her kindness and hospitality. I also thank Ms. Mari Hayashi for her encouragement and various secretarial work.

Finally I express my great thanks to my parents, Koshichi and Yuko Sawada, and my grandmother, Yoko Ozaki, for their continuous encouragement and support during my university days. I would like to dedicate this thesis to my deceased grandfather, Dr. Hiroshi Ozaki, who died in 1994 while he was looking forward the completion of this work.

Appendix A

One-nucleon-exchange Model

In the one-nucleon-exchange model, the differential cross section for the np $\rightarrow$ d$(\pi\pi)^0$ reaction is defined by

$$d\sigma = \frac{m^2}{32\pi^2 p\sqrt{s}}\frac{1}{4}\sum_{\lambda\mu_1\mu_2}|\mathcal{F}_{\lambda\mu_1\mu_2}(s,s_{12},t_3,u_3)|^2\frac{d^3q_1}{E_1}\frac{d^3q_2}{E_2}\frac{d^3q_3}{E_3}\times\delta^4(p_1+p_2-q_1-q_2-q_3), \tag{A.1}$$

where the full scattering amplitudes are assumed to be a product of the Born amplitudes of $np \rightarrow \sigma d$ (F^B) and the decay amplitudes of $\sigma \rightarrow d(\pi\pi)^0$ (F^d):

$$\mathcal{F}_{\lambda\mu_1\mu_2} = F^B_{\lambda\mu_1\mu_2}\cdot F^d(s_{12}). \tag{A.2}$$

Here λ, μ_1 and μ_2 are the helicities of the deuteron neutron and proton, respectively. The variables in the amplitudes are the Lorentz invariants defined by $s = (p_1+p_2)^2$, $s_{12} = (q_1+q_2)^2$, $t3 = (p_1-q_3)^2$ and $u_3 = (p_2-q_3)^2$, where p_1 and p_2 are the 4-momentum of the neutron and the proton respectively, q_3 is the 4-momentum of the deuteron and q_1 and q_2 are the 4-momenta of pions.

The helicity amplitudes $F^B_{\lambda\mu_1\mu_2}$ are calculated using the six invariant amplitudes A^B_i in the Born approximation:

$$F_{\pm1(1/2)(1/2)}(s,s_{12},t_3,u_3) = \mp\frac{\sin\theta}{\sqrt{2}}\left(\frac{p^2}{m}A_2 + pk\cos\theta A_4 + A_5 + \frac{-p^0d^0\pm pk}{m}A_6\right),$$

$$\begin{aligned} F_{0(1/2)(1/2)}(s,s_{12},t_3,u_3) &= -\frac{kpp^0}{mM}A_1 + \frac{p^2d^0}{mM}\cos\theta A_2 - \frac{p^0k^2}{M}\cos\theta A_3 \\ &\quad + \frac{kpd^0}{M}\cos^2\theta A_4 + \frac{d^0}{M}\cos\theta A_5 - \frac{p^0M}{m}\cos\theta A_6, \end{aligned}$$

$$F_{\pm 1(1/2)(-1/2)}(s,s_{12},t_3,u_3) = \frac{1\pm\cos\theta}{\sqrt{2}}\left(\pm\frac{pp^0k}{m}(1\mp\cos\theta)A_4 - \frac{p^0}{m}A_5 + d^0A_6\right),$$

$$F_{0(1/2)(-1/2)}(s,s_{12},t_3,u_3) = \frac{p^0d^0}{mM}\sin\theta\left(-\frac{p^0k^2}{d^0}A_3 + pk\cos\theta A_4 + A_5 - \frac{mM^2}{p^0d^0}A_6\right), \tag{A.3}$$

where m and M are the nucleon and deuteron masses, respectively. The other helicity amplitudes are obtained by using the parity conservation relation

$$F_{\lambda\mu_1\mu_2}(s,s_{12},t_3,u_3) = F_{-\lambda-\mu_1-\mu_2}(s,s_{12},t_3,u_3). \tag{A.4}$$

In these expressions, p, k, p^0 and d^0 denote the quantities in the overall center-of-mass system and are given by

$$\begin{aligned} p &= P(s,m^2,m^2),\\ k &= P(s,M^2,s_{12}),\\ p^0 &= E(s,m^2,m^2),\\ d^0 &= E(s,M^2,s_{12}), \end{aligned} \tag{A.5}$$

with

$$P(x,y,z) = \left(\frac{x^2+y^2+z^2-2xy-2yz-m2zx}{4x}\right)^2,$$

$$E(x,y,z) = \left(\frac{x+y-z}{2\sqrt{x}}\right). \tag{A.6}$$

θ is the scattering angle of the deuteron in the same system and

$$\cos\theta = \frac{2p^0d^0 - m^2 - M^2 + t_3}{2kp}. \tag{A.7}$$

A_i^B are as,

$$A_1^B = -2g_\sigma\left[\frac{R_1(t_3)}{m^2-t_3} - \frac{R_1(u_3)}{m^2-u_3}\right],$$

$$A_2^B = 2g_\sigma\left[\frac{R_2(t_3)}{m^2-t_3} + \frac{R_2(u_3)}{m^2-u_3}\right],$$

$$A_3^B = g_\sigma\left[\frac{R_3(t_3)}{m^2-t_3} + \frac{R_3(u_3)}{m^2-u_3}\right],$$

$$A_4^B = -g_\sigma \left[\frac{R_4(t_3)}{m^2 - t_3} - \frac{R_4(u_3)}{m^2 - u_3} \right],$$

$$A_5^B = 0,$$

$$A_6^B = g_\sigma \left[\frac{R_6(t_3)}{m^2 - t_3} + \frac{R_6(u_3)}{m^2 - u_3} \right], \tag{A.8}$$

where R_i are the function of the deuteron form factor G_i at dpn vertex defined $R_1(t) = G_a(t) - mG_b(t)$, $R_3(t) = -R_4(t) = G_b(t)$, and $R_6(t) = G_a(t)$. In the calculations shown in this paper, the values of $G_a(t)$ and G_b of the solution 2 by Locher *et al.* [35] is used.

The decay amplitudes $F^d(s_{12})$ are calculated from the s-wave $\pi\pi$ phase shift with I = 0 $\delta_{\pi\pi}$ as,

$$F^d(s_{12}) = \frac{1}{q^*(s_{12})} exp(i\delta_{\pi\pi}(s_{12})) \sin \delta_{\pi\pi}(s_{12}), \tag{A.9}$$

where $q^*(s_{12})$ is the magnitude of the pion momentum in the pion rest frame.

Bibliography

[1] I. Bar-Nir, E. Burkhardt, H. Oberlack, A. Putzer, P. Ang, G. Alexander, O. Benary, S. Dagan, J. Grunhaus, L. D. Jacobs, A. Levy, D. Lissauer and I. Stumer, Nucl. Phys. B54 (1973) 17.

[2] A. Abdivaliev, C. Besliu, F. Cotorobai, A. P. Gasparian, S. Gruia, A. P. Ierusalimov, D. K. Kopylova, V. I. Moroz, A. V. Nikitin and Yu. A. Troyan, Nucl. Phys. B168 (1980) 385.

[3] F. Plouin, J. Duflo, L. Goldzahl, G. Bizard, F. Bonthonneau, M. Cottereau, J. L. Laville, C. Le Brun, F. Lefebvres, J. C. Malherbe and R. Regimbart, Nucl. Phys. A302 (1978) 413.

[4] F. Plouin, P. Fleury and C. Wilkin, Phys. Rev. Lett. 65 (1990) 690.

[5] A. Abashian, N. E. Booth, K. M. Crowe, R. E. Hill and A. H. Rogers, Phys. Rev. 132 (1963) 2296.

[6] J. Banaigs, J. Berger, L. Goldzahl, T. Risser, L. Vu Hai, M. Cottereau and C. Le Brun, Nucl. Phys. B67 (1973) 1.

[7] C. L. Hollas, C. R. Newsom, P. J. Riley, B. E. Bonner and G. Glass, Phys. Rev. C 25 (1982) 2614.

[8] H. Yoshino, J. Nagata, M. Matsuda, N. Hiroshige and T. Ueda, Prog. Theor. Phys. 95 (1996) 353, and private communications.

[9] P. Estabrooks and A. D. Martin, Nucl. Phys. B79 (1974) 301.

[10] L. Rosselet, P. Extermann, J. Fischer, O. Guisan, R. Mermod, and R. Sachot, Phys. Rev. D 15 (1977) 574.

[11] A. Zylbersztejn, P. Basile, M. Bourquin, J. P. Boymond, A. Diamant-Berger, P. Extermann, P. Kunz, R. Mermod, H. Suter and R. Turlay, Phys. Lett. 38B (1972) 457.

[12] C. D. Froggatt and J. L. Petersen, Nucl. Phys. B129 (1977) 89.

[13] T. Risser and M. D. Shuster, Phys. Lett. 43B (1973) 68.

[14] I. Bar-Nir, T. Risser and M. D. Shuster, Nucl. Phys. B87 (1975) 109.

[15] H.Noumi, S. Sawada, T. Hasegawa, N. Horikawa, M. Ieiri, M. Ishii, S. Ishimoto, T. Iwata, Y. D. Kim, Y. Katoh, M. Kawabata, M. A. Kovash, M. Minakawa, Y. Mizuno, F. Nakayama, H. Ogami, A. Ogawa, T. Sasaki, T. -A. Shibata, Y. Suzuki, M. Takasaki, K. Tamura, K. H. Tanaka, J. Trice and Y. Yamanoi, in print in Nucl. Instrum. Methods A.

[16] T.Sasaki, T. Hasegawa, S. Hirata, N. Horikawa, S. Ishimoto, T. Iwata, M. Kawabata, Y. D. Kim, M. A. Kovash, Y. Miyachi, Y. Mizuno, F. Nakayama, H. Ogami, A. Ogawa, S.Sawada, T. -A. Shibata, K Tamura and J. Trice, Nucl. Instrum. Methods A 364 (1995) 171.

[17] G. Bizard, F. Bonthonneau, J. L. Laville, F. Lefebvres, J. C. Malherbe, R. Regimbart, J. Duflo and F. Plouin, Nucl. Instrum. Methods III (1973) 451.

[18] CERN Application Software Group, GEANT - Detector Description and Simulation Tool, CERN Long Write-up W5013, Geneva 1993.

[19] M. Ieiri, M. Minakawa, H. Noumi, Y. Yamanoi, Y. Kato, H. Ishii, K. H. Tanaka, Y. Suzuki, M. Takasaki, J. Chiba, M Numajiri, T. Miura, T. Suzuki and K. Kondo, Proc. The 9th Symposium on Accelerator Science and Technology, Tsukuba, Japan, 1993, p.477.

[20] M. Numajiri, T. Miura, Y. Oki, T. Suzuki, K. Kondo, K. H. Tanaka, M. Ieiri, H. Noumi, Y. Yamanoi and M. Takasaki, Proc. The 9th Symposium on Accelerator Science and Technology, Tsukuba, Japan, 1993, p.428.

[21] J. Banaigs et al., Nucl. Instrum. Methods 95 (1971) 307.

[22] K. Kozma and J.Kliman, J. Phys. G: Nucl. Part. Phys. 16 (1990) 45.

[23] G. Bizard et al., Nucl. Instrum. Methods III (1975) 445; R. Lander et al., Phys. Rev. 137B (1965) 1228; Bevalac Users' Manual, pp.II-8.

[24] J. Chiba, T. Kobayashi, T. Nagae, I. Arai, N. Kato, H. Kitayama, A. Manabe, M. Tanaka, K. Tomizawa, D. Beatty, G. Edwards, C. Glashauser, G. J. Kumbartzki, and R. D. Ransome, Phys. Rev. Lett. 67 (1991) 1982.

[25] "TKO Specification", presented by KEK Data Acquisition Development Working Group, KEK-85-10.

[26] KEK report.

[27] J. Myrheim and L. Bugge, Nucl. Instrum. Methods 160 (1979) 43.

[28] G. Bizard, F. Bonthonneau, J. L. Laville, F. Lefebvres, J. C. Malherbe and R. Regimbart, Nucl. Phys. B85 (1975) 14.

[29] R. E. Mischke, P. F. Shepard and T. J. Devlin, Phys. Rev. Lett. 23 (1969) 542

[30] E. L. Miller, M. Elfield, N. W. Reay, N. R. Stanton, M. A. Abolins, M. T. Lin, and K. W. Edwards, Phys. Rev. Lett. 26 (1971) 984

[31] M. B. Davis, B. G. Gibbard, M. N. Kreisler, T. Dobrowolski, M. J. Longo, D. D. O'Brien and T. Toohig, Phys. Rev. Lett. 29 (1972) 139.

[32] R. M. Heinz, O. E. Overseth, D. E. Pellett and M. L. Perl, Phys. Rev. 167 (1968) 1232.

[33] H. L. Anderson, D. A. Larson, L. C. Myrianthopoulos, L. Dubal, C. K. Hargrove, E. P. Hincks, R. J. McKee, H. Mes, D. Kessler and A. C. Thompson, Phys. Rev. D 9 (1974) 580.

[34] R. Machleidt, K. Holinde and Ch. Elster, Phys. Rep. 149 (1987) 1.

[35] M. P. Locher and A. Švarc, Z. Phys. A338 (1991) 89.